Journal of
Composites Science

Article

Microwave-Assisted Hydrothermal Synthesis of Cu/Sr-Doped Hydroxyapatite with Prospective Applications for Bone Tissue Engineering

Diana-Elena Radulescu [1], Bogdan Stefan Vasile [2,3,4], Otilia Ruxandra Vasile [1,3,4], Ionela Andreea Neacsu [1,3,*], Roxana Doina Trusca [3], Vasile-Adrian Surdu [5], Alexandra Catalina Birca [2,3], Georgiana Dolete [1,3], Cornelia-Ioana Ilie [1,3] and Ecaterina Andronescu [1,3,4,*]

[1] Department of Science and Engineering of Oxide Materials and Nanomaterials, Faculty of Chemical Engineering and Biotechnologies, National Polytechnic University of Science and Technology of Bucharest, 011061 Bucharest, Romania
[2] Advanced Research Center for Innovative Materials, Products and Processes, National Polytechnic University of Science and Technology of Bucharest, 011061 Bucharest, Romania
[3] National Research Center for Micro and Nanomaterials, National Polytechnic University of Science and Technology of Bucharest, 060042 Bucharest, Romania
[4] Romanian Academy of Scientists, 050045 Bucharest, Romania
[5] Department of Materials Science, Faculty of Materials Science and Engineering, Transilvania University of Brasov, 29 Eroilor Blvd., 500036 Brasov, Romania
* Correspondence: ionela.neacsu@upb.ro (I.A.N.); ecaterina.andronescu@upb.ro (E.A.)

Academic Editors: Julfikar Haider and Swadesh Kumar Singh

Received: 27 June 2025
Revised: 2 August 2025
Accepted: 5 August 2025
Published: 7 August 2025

Citation: Radulescu, D.-E.; Vasile, B.S.; Vasile, O.R.; Neacsu, I.A.; Trusca, R.D.; Surdu, V.-A.; Birca, A.C.; Dolete, G.; Ilie, C.-I.; Andronescu, E. Microwave-Assisted Hydrothermal Synthesis of Cu/Sr-Doped Hydroxyapatite with Prospective Applications for Bone Tissue Engineering. *J. Compos. Sci.* **2025**, *9*, 427. https://doi.org/10.3390/jcs9080427

Abstract

One of the main challenges in hydroxyapatite research is to develop cost-effective synthesis methods that consistently produce materials closely resembling natural bone, while maintaining high biocompatibility, phase purity, and mechanical stability for biomedical applications. Traditional synthetic techniques frequently fail to provide desirable mechanical characteristics and antibacterial activity, necessitating the development of novel strategies based on natural precursors and selective ion doping. The present study aims to explore the possibility of synthesizing hydroxyapatite through the co-precipitation method, followed by a microwave-assisted hydrothermal maturation process. The main CaO sources selected for this study are eggshells and mussel shells. Cu^{2+} and Sr^{2+} ions were added into the hydroxyapatite structure at concentrations of 1% and 5% to investigate their potential for biomedical applications. Furthermore, the morpho-structural and biological properties have been investigated. Results demonstrated the success of hydroxyapatite synthesis and ion incorporation into its chemical structure. Moreover, HAp samples exhibited significant antimicrobial properties, especially the samples doped with 5% Cu and Sr. Additionally, all samples presented good biological activity on MC3T3-E1 osteoblast cells, demonstrating good cellular viability of all samples. Therefore, by correlating the results, it could be concluded that the undoped and doped hydroxyapatite samples are suitable biomaterials to be further applied in orthopedic applications.

Keywords: hydroxyapatite; doping; strontium; copper; biological activity; morpho-structural properties

1. Introduction

In the last decade, studies focused on the most problematic issue concerning hard tissue engineering, namely the enhancement of osseous tissue regeneration for tissue damage generated by accidents or diseases. While the human body possesses the capacity to produce new osseous tissue, this ability is highly influenced by the size of the damaged area. In this regard, various solutions have been investigated to avoid any secondary surgeries by applying innovative materials to develop bone scaffolds or implants for tissue regeneration enhancement. Moreover, the selected materials should also possess increased biocompatibility and good antibacterial capacity to prevent bacterial infections [1,2].

Hydroxyapatite (HAp), with the chemical composition $Ca_{10}(PO_4)_6(OH)_2$, is known as the main component of the native tissue and the mineral part of the bone. In this direction, HAp is preferred in hard tissue applications for its biocompatibility, non-toxicity, and osteogenic properties. Its good osteoconductivity and osteoinductivity favor HAp to be applied for the enhancement of bone formation. Further, researchers demonstrated that HAp led to an increase in local Ca^{2+}. HAp is also known to activate osteoblast proliferation, promoting the growth and differentiation of mesenchymal stem cells (MSCs). Until this moment, this ceramic material has been widely applied as pure HAp, ion-doped, or introduced into polymer composites. However, pure HAp presents poor mechanical properties, fragility, and a tendency to aggregate [3]. Researchers have focused on optimizing different synthesis strategies to increase HAp's low mechanical properties and poor antibacterial properties [4]. In this regard, HAp can be obtained from not only synthetic but also natural sources. By considering the chemical synthesis route, the synthesized HAp presents brittleness, an unbalanced stoichiometric ratio, and uses hazardous chemicals [5].

On the other side, HAp obtained by using biogenic sources is free from contamination, presents great crystallinity, and is eco-friendly. Studies have shown that synthetic HAp has decreased biodegradability compared to natural-based HAp. Natural-source HAp has been considered for bone grafts, implants, coatings, and composite materials, demonstrating superior biocompatibility and mechanical properties when compared to synthetic HAp. Additionally, HAp obtained from natural sources demonstrated enhanced biocompatibility and antibacterial characteristics, recommending it for biomedical applications [6]. In this regard, Cursaru [7] demonstrated promising potential for biomedical applications, particularly in bone implants. The material exhibits enhanced mechanical properties, including high hardness and compressive strength, which exceed those of natural bone, as well as favorable wear resistance. Furthermore, the observed increase in cell viability and proliferation confirms its biocompatibility, making it a strong candidate for use in bone repair and replacement devices. Further, Wu et al. [8] confirmed that nano-HAp produced from oyster shells using the hydrothermal technique has great potential for orthopedic and biological applications. The developed materials improved fracture toughness and microhardness while incorporating beneficial trace elements, indicating a high potential for usage in bone repair, regeneration, and implantable devices. Furthermore, using oyster shells as a sustainable CaO source promotes the production of biomedical materials that are both environmentally friendly and cost-effective. At the same time, Pon-On et al. [9] mentioned that naturally derived HAp exhibited enhanced cell adhesion, proliferation, and differentiation, but also high non-toxicity compared to synthetic HAp. Moreover, Nam et al. [10] highlighted that the biological HAp presents various trace elements in its structure, such as Mg^{2+}, K^+, Zn^{2+}, Na^+, Sr^{2+}, etc., which are essential in bone formation, regeneration, and remodeling processes. Moreover, new hybrid materials integrate bio-HAp with synthetic HAp nanoparticles to benefit from the advantages of both types of materials, such as increased cell interaction and osteogenic potential [11].

Besides the synthesis methods, the mechanical and biological properties of HAp can also be improved by modifying its crystallographic structure [12]. A versatile structure permits the substitution of anions and cations to change numerous properties of the obtained material but also expands the functionality of HAp in hard tissue engineering.

This substitution can be performed in three different sites in the crystal structure, such as Ca^{2+} ions, PO_4^{3-} ions, or at the OH^- site [13,14]. Furthermore, natural HAp was proven to efficiently substitute anions (CO_3^{2-}, PO_4^{-3}, F^-, Cl^-, and SiO_4^{4-}) or cations (Co^{2+}, Ni^{2+}, Ag^+, Sr^{2+}, Zn^{2+}, Mg^{2+}, and Fe^{3+}) because of its ingrained calcium deficiency [15–17]. Additionally, by doping the material with other metals, thermal stability, lattice parameters, crystallinity, and morphology are influenced, significantly shaping the solubility of doped HAp in the physiological environment. Therefore, the structure of the obtained biomaterial offers suitable support for angiogenesis and bone tissue growth on implanted sites [18,19]. At the same time, different types of ion doping agents can also enhance the biological characteristics of HAp, such as anti-tumor activity, antibacterial properties, and bone induction [20].

Ion-doping of HAp with metallic ions was proven to be a promising path to mimic the biological apatite, but also to stimulate a definite biological response in the human body, such as increased antimicrobial activity, cell proliferation, osteogenesis, and angiogenesis [21]. To confirm this, Dorcioman et al. [22] reported on the effective synthesis of HAp-based thin film coatings obtained from marine biowaste, such as salmon fish bones and seashells, via pulsed laser deposition. The developed coatings, both undoped and doped, demonstrated outstanding adhesion, bioactivity, cytocompatibility, and antibacterial properties, all of which are important for biomedical applications. These findings suggest that sustainable marine-derived HAp coatings are extremely appealing possibilities for next-generation dental and orthopedic implant surfaces, providing both biological performance and resistance to microbial colonization. Further, Singh et al. [23] mentioned that metal ions doping into the structure of HAp led to cell proliferation and differentiation, enhancing bone formation. In this direction, strontium (Sr^{2+}) ions present a similar structure to Ca^{2+} ions, being a trace element generally found in the human body, with high importance for bone development, showing great efficacy in inducing osteoblast activity [24,25]. Sr can promote osseous tissue formation and reduce bone self-absorption while exhibiting an effective ability to increase osteoblast differentiation and at the same time inhibit osteoclast activity. The similarity between Ca^{2+} and Sr^{2+} ions enables the possibility for Sr to substitute Ca in the HAp structure. This modification demonstrated an improved biological effect for the ceramic material. Hence, the use of Sr-doped HAp in hard tissue engineering is, without doubt, an ideal solution to improve the efficiency of bone regeneration [26]. Zhu's research group [27] also mentioned that Sr-substituted HAp exhibited enhanced biocompatibility, bioactivity, osteoconduction, degradation rate, and mechanical performance. Additionally, small doses of Sr were demonstrated to play an important role in bone formation, the control of bone resorption, bone cancer treatment, and bone pain relief, illustrating its importance for the incorporation into the structure of HAp materials.

Another doping ion highly recommended for the substitution into the HAp structure is represented by copper (Cu), which can also be found in the human body. Besides its antibacterial effect, it possesses an important role in the cross-linking of bone elastin and collagen, exhibiting limited cytotoxicity [28,29]. The substitution of HAp with Cu^{2+} induces the antibacterial capacity of HAp materials, by reducing the risk of inflammation after its application in biomedical applications. Furthermore, these doping ions encourage osteogenic differentiation, protein absorption, and bone-like apatite nucleation and growth at the implantation site. All these effects accelerate the healing process and the growth of novel osseous tissue [30].

Lately, most studies have focused on the effects of synthesis methods of HAp using biogenic sources without affecting the chemical composition. In this regard, Irfa'I et al. also confirmed that the development of HAp from biogenic sources has been the most challenging aspect, since biological appetites have a more nonstoichiometric and less crystalline structure [31].

To surpass this issue, subsequent treatments are needed to obtain the stoichiometric Ca/P ratio of 1.67 and improved crystallinity.

Unlike previous studies that mainly focused on the use of synthetic sources for HAp production, this research aims to explore the utilization of naturally derived materials. Likewise, an additional aspect of novelty is represented by doping of the obtained HAp material. The biological potential of the synthesized doped HAp has not been extensively explored in previous research, while the purpose of this study is to demonstrate the combination of the use of natural sources for HAp synthesis and ion substitution. This innovative approach was introduced as having significant potential to advance future applications in biomedical engineering. This study aimed to obtain HAp by using biogenic sources (eggshells and mussel shells), doped with different metal ions in different concentrations. For ion substitution, Cu and Sr were selected. Further, the obtained samples were investigated considering their morpho-structural properties and biological activity, namely the cellular viability and antimicrobial effect.

2. Materials and Methods

2.1. Materials

Mussel shells and eggshells were procured from a local restaurant to be used as calcium oxide sources. For the synthesis of doped HAp, the following precursors were used: $(NH_4)_2HPO_4$ (98%), NH_4OH, $Sr(NO_3)_2$ (98%), $Cu(NO_3)_2 \times 2.5H_2O$ from Sigma–Aldrich, Saint Luis, MO, USA, and distilled water. Nutrient broth No 2, Sabouraud broth, agar, methanol, crystal violet, and acetic acid (Sigma–Aldrich, Saint Luis, MO, USA) were utilized for antimicrobial assays. Additionally, the strains tested in this study are standard reference strains obtained from the American Type Culture Collection (ATCC)—*Staphylococcus aureus* ATCC 25923, *Enterococcus faecalis* ATCC 29212, *Escherichia coli* ATCC 25922, *Pseudomonas aeruginosa* ATCC 27853, *Candida albicans* ATCC 10231, and *Candida parapsilosis* ATCC 22019—and are part of the Microorganisms Collection of the Department of Science and Engineering of Oxide Materials and Nanomaterials. Further, fetal bovine serum, DMEM medium (Sigma-Aldrich, Saint Luis, MO, USA), and XTT reagent (2,3-Bis-(2-Methoxy-4-Nitro-5-Sulfophenyl)-2H-Tetrazolium-5-Carboxanilide) (Thermo Fischer Scientific, Waltham, MA, USA) were used for the XTT Cell Viability Assay.

2.2. CaO Preparation

The obtained mussel shells were cleansed with boiled water to remove the impurities attached to the shells. Further, the shells were washed with distilled water and introduced into the ultrasonic bath to remove any residues left. After washing, shells were dried in the oven at 60 °C for 48 h and ground until a fine powder had been obtained. The resulting powder was heat-treated at 1000 °C for 3 h. As for the eggshells, their membrane was first removed by immersing them in a 0.5 M HCl solution. After the removal of the organic parts, the same process used for mussel shells was applied. The rigorous cleaning and heat treatment approach used in this study was specifically designed to effectively remove organic and inorganic contaminants from natural sources. Our prior study by the same research group [32] confirmed the efficacy of this purification method using complete elemental analysis. As demonstrated in our previous study, the final CaO products derived from both eggshells and mussel shells following this treatment approach included negligible contaminants, with trace elements remaining significantly below detection limits or within acceptable levels for biomedical applications.

2.3. Undoped HA and Cu/Sr-Doped Hydroxyapatite Synthesis Method from Biogenic Sources

HAp synthesis was performed through the co-precipitation method, followed by a microwave-assisted hydrothermal maturation process with the aid of the synthWAVE equipment (Milestone Srl, Sorisole, Bergamo, Italy). This method was selected due to its capacity to change the nucleation and crystal growth in specific conditions, such as controlled pressure and increased temperature. Researchers reported that with the aid of microwaves, the synthesis process is fast and more effective. Furthermore, the obtained materials present good dispersibility and crystallinity [33–35].

For the co-precipitation, a solution of $(NH_4)_2HPO_4$ was prepared by dissolving 11.04 g in 200 mL of distilled water, while 7.8 g of CaO was dispersed in 200 mL of distilled water. For the experiments, both CaO obtained from eggshells and mussel shells were used. The phosphate solution was added dropwise into the Ca^{2+} dispersion under magnetic stirring at room temperature. During the precipitation, the pH was set at around 9–10. After obtaining the desired pH value, the mixture was transferred into the vessel of microwave-assisted equipment and subjected to hydrothermal maturation.

The microwave-assisted hydrothermal synthesis method was set up in specific conditions, with an initial pressure of 2 bars; in 2 min, the temperature increased to 120 °C and remained constant for the following 10 min. After the maturation process, the resulting precipitates were filtered and washed with distilled water until a neutral pH was reached, and then dried in the oven at 60 °C for 48 h. For the Sr/Cu-doped HAp, the process was similar to undoped HAp synthesis. The only difference is presented by the addition of the substituents precursors: $Sr(NO_3)_2$ or $Cu(NO_3)_2$. To obtain Sr-doped HAp and Cu-doped HAp, various quantities of precursors were used corresponding to different Ca^{2+} substitution molar ratios (1% and 5%). Based on findings in the literature [36–38] 1% and 5% molar concentrations of Sr^{2+} and Cu^{2+} were chosen. According to research, higher concentrations of Sr can cause cytotoxicity, and concentrations between 1% and 3% have been demonstrated to efficiently increase osteoblast activity while preserving biocompatibility [39]. For Cu, concentrations above 5% can be toxic, whereas suitable concentrations of Cu ($\leq$1%) have demonstrated optimum antibacterial properties without causing any negative side effects [40–42]. Both 1% and 5% are frequently used in the literature to find a balance between functional modification and structural stability. Furthermore, these are strong enough to generate identifiable changes in physical properties (particle size, band gap, or catalytic activity), but sufficiently small to preserve the primary crystallographic phase of the material while preventing disadvantages such as agglomeration or metallic cluster formation [43]. Separate solutions of corresponding precursors were added to the CaO dispersion, under magnetic stirring, before the addition of phosphate solution. The obtained solutions followed the same process of hydrothermal maturation in the microwave field. Based on the source of the natural source and doping ion, the samples were named as mentioned in Table 1.

Table 1. Codification of the synthesized samples (1% and 5% represent the concentrations of the doping ions).

Source	Code
Eggshell (C)	HAp_C HAp_Cu_1_C HAp_Cu_5_C HAp_Sr_1_C HAp_Sr_5_C HAp_S

Table 1. *Cont.*

Source	Code
Mussel shells (S)	HAp_Cu_1_S HAp_Cu_5_S HAp_Sr_1_S HAp_Sr_5_S

2.4. Characterization Methods

2.4.1. X-Ray Diffraction (XRD)

The phase composition, crystallinity, and unit cell parameters investigation of the obtained samples were extracted from X-ray diffraction patterns performed using CuKα radiation-provided PANalytical Empyrean equipment (PANalytical, Almelo, The Netherlands). The obtained diffractograms were acquired between the 2θ angle values of 20 and 80°, with a 0.0256° step size and 255 s time per step. Further, the diffractograms were fitted using the Rietveld refinement algorithm, using a polynomial function for background approximation, a pseudo-Voigt function for peak profile, and a Caglioti function for peak width approximation with the aid of the HighScore Plus software (version 3.0, PANalytical, Almelo, The Netherlands) and the ICDD PDF4+ 2022 database. For the refinement of the obtained diffractograms, a goodness of fit < 4 was considered acceptable to determine the structural parameters and the crystallinity of each sample. Thus, quantitative phase composition, unit cell parameters, and crystallinity were obtained.

2.4.2. Scanning Electron Microscopy (SEM)

To investigate the morphology of the obtained samples, a QUANTA INSPECT F50 scanning electron microscope (Thermo Fisher, Eindhoven, The Netherlands) was used for scanning electron microscopy (SEM). The microscope was equipped with a field electron emission gun (FEG), with a resolution of 1.2 nm, and an EDS (Energy Dispersive Spectroscopy) (Thermo Fisher, Eindhoven, The Netherlands). detector, with a resolution at MnK of 133 eV. The powder samples were fixed on a carbon-bearing slide and introduced into an analysis chamber. The HAp particle size distribution was investigated with the use of ImageJ software (Version 1.53e, National Institutes of Health, Bethesda, MD, USA).

2.4.3. Transmission Electron Microscopy (TEM)

Transmission electron microscopy (TEM) analyses were performed using a Titan Themis 200 microscope (Thermo Fisher, Eindhoven, The Netherlands), operating at an accelerating voltage of 200 kV. This advanced instrument is equipped with a high-brightness X-FEG Schottky field emission gun and integrates a Super-X EDX detector system for rapid and sensitive elemental mapping, complemented by an Enfinium electron energy loss spectroscopy (EELS) detector for detailed chemical state analysis, including light elements.

2.4.4. Fourier-Transform Infrared Spectroscopy (FT-IR)

A Thermo Scientific Nicolet iS50 (Thermo Fischer Scientific, Waltham, MA, USA) spectrometer was used for the acquisition of IR spectra to assess the functional groups present in the obtained materials. The acquisitions were made at room temperature, with a resolution of 4 cm^{-1}, 64 scans for each sample, at the 4000–400 cm^{-1} wavenumber range. It was able to record the data obtained by connecting the spectrometer to a data collection and processing device using the Omnic work program. (Thermo Nicolet, Version 8.2).

2.4.5. Inductively Coupled Plasma–Mass Spectrometry (ICP-MS)

The elemental analysis of the obtained HAp powders from natural sources was performed using an Agilent 8800 Triple Quadrupole ICP-MS (Agilent Technologies, Tokyo, Japan), equipped with an ASX500 autosampler (Agilent Technologies, Tokyo, Japan), MicroMist concentric nebulizer (Agilent Technologies, Tokyo, Japan), Peltier cooling spray-chamber (Agilent Technologies, Tokyo, Japan) set at a temperature of 2 °C, a torch with an internal diameter of 2.5 mm, and Ni sampler and skimmer cones. The equipment was adjusted following the specifications provided by the manufacturer and calibrated using a set of five calibration standards, having a concentration range between 1 and 100 μg/L for each investigated element. The analysis was performed to detect the presence of other traces of metals existing in the HAp powder from the biogenic sources used in the synthesis, but also the doping of the biogenic-based HAp. The calibration curves for all the metals of interest confirmed a strong linear relationship, as indicated by the correlation coefficients (R^2) exceeding 0.999. Therefore, using the same calibration in the 1–100 μg/L range, the amounts of Li, Be, Al, V, Co, Ni, Cr, Mn, Co, Ni, Zn, As, Cd, and Pb were assessed.

2.4.6. Biological Evaluation

Antimicrobial Assays

The antimicrobial properties of the developed materials were quantitatively assessed using the minimum inhibitory concentration (MIC) method described in a previous study [44] and according to M100-Performance *Standards for Antimicrobial Susceptibility Testing* 35st Edition [45]. MIC evaluation was made via the decimal microdilution method in Nutrient Broth and Sabouraud broth. Microbial cell suspensions were made in a sterile physiological buffer using fresh cultures with 1.5×10^8 CFU/mL. Decimal dilutions were made from each nanoparticle suspension, followed by inoculation with a standard microbial suspension (medium liquid volumetric ratio/microbial suspension = 10:1). Following, the same steps were performed on the blank/control (C) samples for sterility and microbial growth. The 96-well plates were incubated at 37 °C for 24 h. The MIC values were determined by spectrophotometric measurements of absorbance at 620 nm with a FilterMax F5 Multi-mode microplate Reader (Molecular Devices, San Jose, CA, USA) [44].

The microtiter broth assay was performed to evaluate biofilm development on the inert substrate using the same microdilution method presented in a previous study [44]. After 24 h of incubation, the liquid medium from 96-well plates (containing binary dilution of the samples tested) was discarded, the wells were washed three times with sterile physiological buffer, and the bacterial cells adhered to the walls were fixed with cold methanol for 5 min, followed by staining with 1% crystal violet solution for 15 min. The dyed biofilm was resuspended in 33% acetic acid solution, and the absorbance of the blue solution was measured at 490 nm [44].

Biocompatibility Assay

Considering the biological activity of the synthesized undoped and doped HA samples, the biocompatibility was investigated using XTT reagent (2,3-Bis-(2-Methoxy-4-Nitro-5-Sulfophenyl)-2H-Tetrazolium-5-Carboxanilide) according to the manufacturer's protocol (CyQUANT™ XTT Cell Viability Assay Kit, Thermo Fischer Scientific, Waltham, MA, USA). In the assay kit, it is included also the Electron Coupling Reagent and XTT reagent. The XTT reagent is represented by a tetrazolium-based compound sensitive to the cellular redox potential. The water-soluble XTT compound is converted by the actively viable cells into an orange-colored formazan product. The consistency and sensitivity of the analysis were substantially amplified when it was used with the Electron Coupling Reagent. The MC3T3 cell line was grown in DMEM medium (Sigma-Aldrich, Saint Luis, MO, USA) supplemented with 1% antibiotics (penicillin and streptomycin) and 10% fetal bovine serum (Sigma-Aldrich, Saint Luis, MO, USA), which was changed twice a week. The cells were put in 96-well plates, at a density of 3000 cells/well in the presence of undoped and doped HA samples for 24 h and 48 h. Further, the control samples were represented only by cells cultivated in identical conditions, but without the presence of synthesized samples. Subsequently, 70 µL of XTT solution was added to the cells, followed by incubation at 37 °C for 4 h. After vigorous homogenization of formazan crystals, the absorbance was read at 450 nm using a spectrophotometer.

2.5. Statistical Analysis

The data were statistically analyzed using GraphPad Prism, version 10.4, from GraphPad Software (San Diego, CA, USA). All experiments were performed in three independent determinations. The results are expressed as ±SD (standard deviation) and analyzed using a one-way analysis of variance (one-way ANOVA) followed by a multiple comparisons assay according to the experimental method. The differences between groups/samples were considered statistically significant when the *p*-value was <0.05.

3. Results

3.1. X-Ray Diffraction (XRD)

Figure 1 shows the diffraction patterns of the obtained samples through the microwave-assisted hydrothermal treatment process. The resulting diffraction data of the undoped sample using eggshells as CaO precursor demonstrated the success of HAp synthesis (ICDD PDF4 + 96-900-2215), with a very small amount of the $Ca(OH)_2$ as secondary phase (ICDD PDF4 + 96-100-0046), while the sample using mussel shells as CaO precursor confirmed HAp synthesis (ICDD PDF4+ 96-900-2214). All doped samples confirmed in their diffraction data the successful synthesis of HAp (Table 1), in agreement with the standard data. In all diffraction patterns for the samples based on eggshells, HAp in the hexagonal crystallization system has been identified, with a $P6_3/m$ space group. Therefore, for all the obtained samples, the principal and sharp diffraction peaks are recognized at 2θ values of 25.82, 31.69, 46.71, and 49.42, corresponding to (0 0 2), (2 1 1), (2 2 2), and (2 1 3) diffraction planes. Similarly, the samples based on mussel shells presenting broader diffraction peaks are highlighted at 2θ values of 25.81, 31.99, 46.76, and 49.39, which correspond to (0 0 2), (2 1 1), (2 2 2), and (2 1 3) diffraction planes. The high similarity to the XRD patterns between undoped and doped HAp samples demonstrates Sr^{2+} and Cu^{2+} substitution in the lattice of the apatite without influencing the chemical structure [46].

Considering the doping ions, through the substitution of Cu^{2+} into the HAp lattice, it has been clearly shown that the crystallinity of the samples decreases, as the peaks broaden and the intensity of the diffraction peaks decreases. This could correspond to the valency of Cu^{2+} when compared with that of phosphorus. The peaks highlighted a small shift towards higher angles in the XRD pattern associated with the modification of the unit cell parameters (Table 2). These parameters are altered due to the doping concentration [47]. As for Sr^{2+} substitution of Ca^{2+} into HAp, the diffraction peaks of doped samples slightly increased, leading to an increase in the crystallinity. However, it was observed that the synthesized materials are well-crystallized compounds. Moreover, it was concluded that, as the dopant concentration increases, the peak intensity decreases significantly, with a slight peak shift of all major peaks. Ion substitutions determine a decrease in the average crystallite size, as shown in Table 3. For eggshell-derived samples, Cu doping showed variable effects on crystallite size, whereas Sr doping resulted in smaller crystallites. Similar trends were observed in mussel shell-derived samples; however, Sr doping gave more variable results. Overall, Sr doping reduced crystallite size relative to undoped samples, while Cu doping had concentration-dependent effects. Furthermore, Sr- and Cu-doping reduces average crystallite size in host lattices by distorting the lattice, increasing strain, and inhibiting grain development. The 1% and 5% molar doping concentrations are commonly regarded as ideal and safe for such research. They consistently change the crystallite structure and characteristics, while preventing excess trap or cluster formation [43].

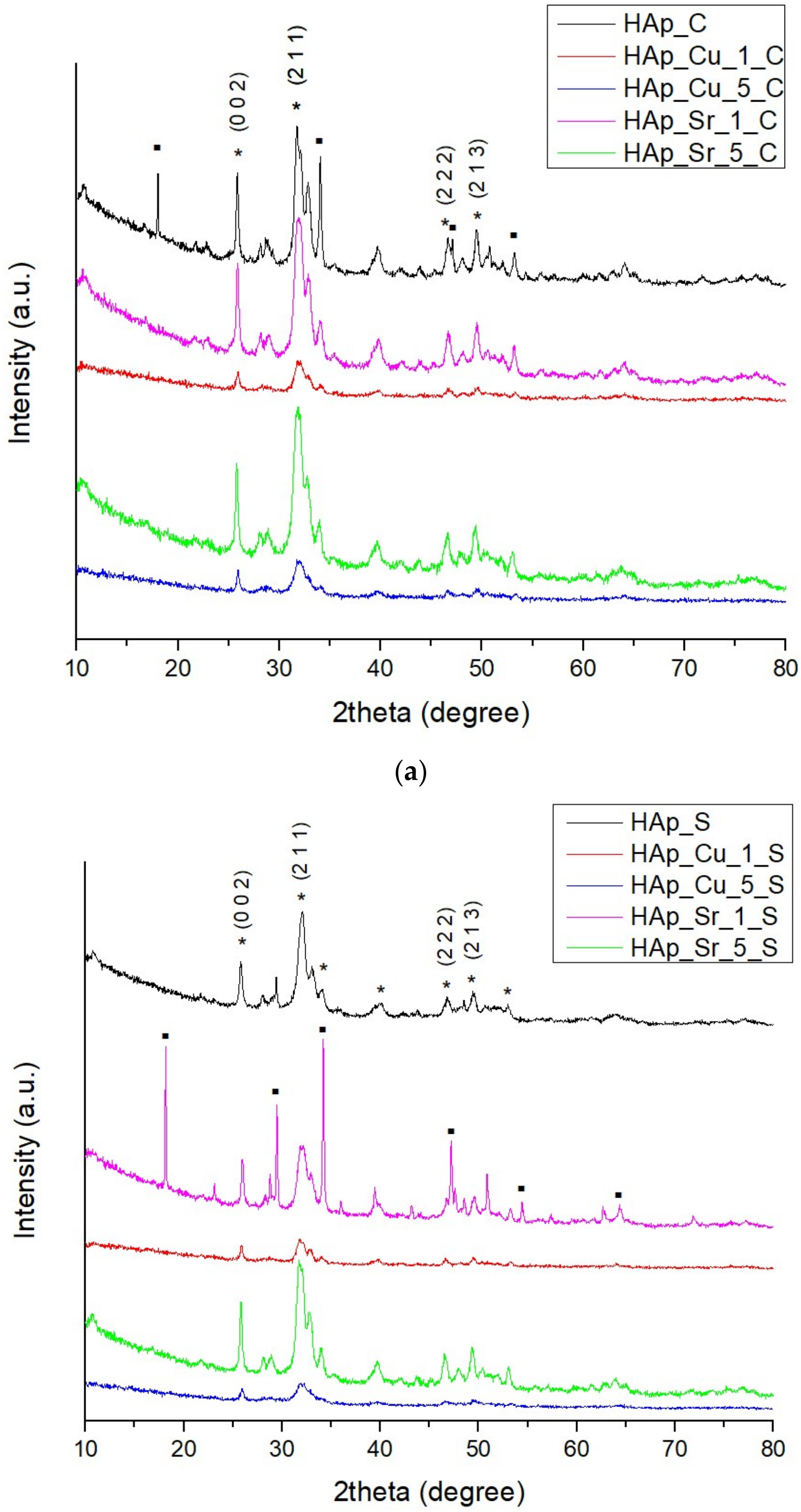

(**a**)

(**b**)

Figure 1. XRD patterns of the doped samples compared to undoped HAp: (**a**) HAp obtained from eggshells, doped with 1% and 5% Cu and Sr; (**b**) HAp obtained from mussel shells, doped with 1% and 5% Cu and Sr. ▪—$Ca(OH)_2$, *—$Ca_{10}(PO_4)_6(OH)_2$.

Table 2. Structural parameters of the crystalline HAp phase present in the synthesized samples, obtained by Rietveld Refinement.

Code	GOF	R Values			Lattice Parameters		
		R_{exp} (%)	R_{wp} (%)	R_p (%)	Unit Cell a (Å)	Unit Cell c (Å)	Unit Cell Volume (Å^3)
HAp_C	2.657	8.596	14.013	11.616	9.429	6.880	529.762
HAp_Cu_1_C	1.062	13.308	13.718	11.275	9.434	6.877	530.176
HAp_Cu_5_C	0.965	12.698	12.480	10.272	9.435	6.874	530.076
HAp_Sr_1_C	2.242	7.892	11.818	9.707	9.430	6.889	530.657
HAp_Sr_5_C	1.600	6.725	8.508	6.754	9.454	6.898	534.699
HAp_S	3.069	8.494	14.882	12.218	9.395	6.918	528.933
HAp_Cu_1_S	1.013	13.257	13.348	10.947	9.436	6.880	530.546
HAp_Cu_5_S	1.059	12.710	13.082	10.632	9.454	6.878	532.480
HAp_Sr_1_S	3.481	7.851	14.651	11.315	9.437	6.886	531.137
HAp_Sr_5_S	1.919	6.888	9.543	7.678	9.453	6.897	534.638

Table 3. Phase content, crystal system, space group, crystallinity, and crystallite size of the obtained samples resulted after Rietveld Refinement.

Code	Phase Content (%)		Crystal System	Space Group	Crystallinity (%)	Average Crystallite Size (nm)
	HAp	Ca(OH)$_2$				
HAp_C	92.2	7.8	Hexagonal	P6$_3$/m	50.6	34.4
HAp_Cu_1_C	100	-	Hexagonal	P6$_3$/m	36.22	23.3
HAp_Cu_5_C	100	-	Hexagonal	P6$_3$/m	41.92	36.6
HAp_Sr_1_C	100	-	Hexagonal	P6$_3$/m	52.08	21.9
HAp_Sr_5_C	100	-	Hexagonal	P6$_3$/m	54.53	24.2
HAp_S	100	-	Hexagonal	P6$_3$/m	49.92	35.4
HAp_Cu_1_S	100	-	Hexagonal	P6$_3$/m	34.4	28.1
HAp_Cu_5_S	100	-	Hexagonal	P6$_3$/m	30.4	35.5
HAp_Sr_1_S	80.9	19.1	Hexagonal	P6$_3$/m	51.53	57.3
HAp_Sr_5_S	100	-	Hexagonal	P6$_3$/m	52.68	25.6

To investigate the lattice parameters and agreement indices of the undoped and doped HAp samples, Rietveld analysis was performed, as shown in Table 3. In this direction, the modifications of unit cell parameters could be observed, as shown in Figure 2, without any changes in the crystal arrangement of the hexagonal structure. Related to the doping ion, the samples doped with Sr^{2+} exhibited increases in the lattice parameters (unit a, c, and unit cell volume) depending on the doping concentration, which confirms their incorporation into the HAp structure into the Ca(1) or Ca(2) site. Peak shifting is also correlated with the increase in lattice parameters. As stated by other researchers, the ionic radii of Sr^{2+} (0.117 nm) are bigger than Ca^{2+} (0.099 nm), inducing strain in the lattice and leading to the shifting of peaks towards decreased diffraction angles [48].

Similarly, Cu^{2+} incorporation into the HAp structure also alters the crystal structure, leading to a reduction of sample crystallization, thus decreasing the crystallinity degree. In all substituted samples, lattice parameters present an increase without disrupting the hexagonal structure. This can also be correlated to the substitution of Ca^{2+} with doping ions that possess a smaller ion radius than the dopant [30]. Unabia et al. [49] explained that Cu^{2+} substitution into Ca sites cannot be performed due to the significant difference between the ionic radii of Cu (0.73 nm) and Ca^{2+} (0.099 nm). As the unit cell presents the most significant modifications, Cu^{2+} is highly likely to be introduced into the HAp structure in interstitial positions along the hexagonal channel.

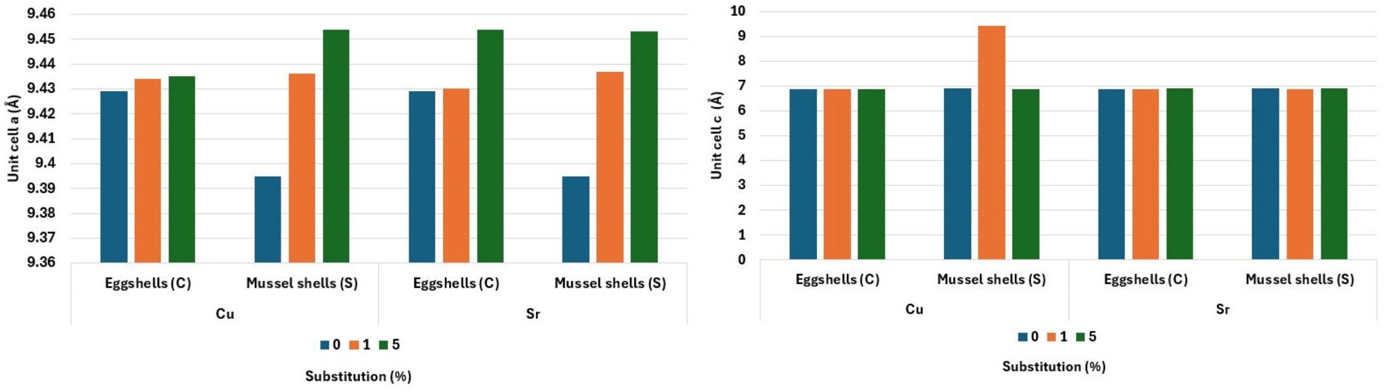

(**a**) unit cell a (**b**) unit cell c

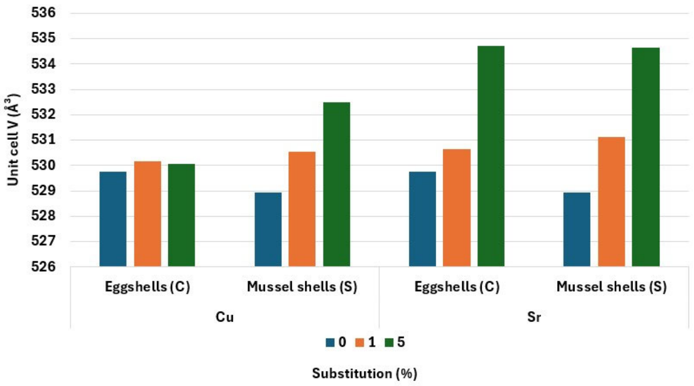

(**c**) unit cell V

Figure 2. Lattice parameter variations of unsubstituted and ion-substituted HAp samples synthesized from eggshells (C) and mussel shells (S): (**a**) unit cell parameter a, (**b**) unit cell parameter c, and (**c**) unit cell volume. Data corresponds to the values presented in Table 2. Blue bars represent undoped samples, orange bars represent 1% doping concentration, and green bars represent 5% doping concentration.

3.2. Scanning Electron Microscopy (SEM)

The morpho-structural characteristic of the obtained samples was determined with the aid of SEM analysis, as shown in Figure 3. SEM micrographs illustrate the elongated shapes of particles. Further, as the doping concentration was increased, the nanoparticles presented an increased tendency to agglomerate. In addition, the morphology of the nanoparticles is modified with the increase in doping concentration. Furthermore, depending on the source of CaO precursor, HAp obtained from eggshells exhibited dimensions between 6 and 25 nm, while HAp obtained from mussel shells presented dimensions between 3 and 17 nm.

The influence of the type of substitute ion and its concentration on HAp samples can also be demonstrated by analyzing the histograms of the synthesized samples. A comprehensive visual and statistical examination of the particle size distributions suggests a predominantly Gaussian (normal) distribution pattern across different doping conditions. From Figure 4, the particle size distributions can be observed. The results demonstrated a predominantly Gaussian distribution pattern across different doping conditions. The undoped samples presented an average particle size of 14.75 ± 1.36 nm for the samples obtained from eggshells and 14.82 ± 1.44 nm for the samples obtained from mussel shells. Also, the particle size decreased by incorporating Cu^{2+} and Sr^{2+} into the HAp lattice. Further, by increasing the ion concentration, the average particle size was reduced. On the other hand, the type of substituting ion also shows a considerable influence on the dimension of the nanoparticle. The Cu^{2+} led to a decrease up to 13.35 ± 1.30 nm and

13.56 ± 1.36 nm, and the increase in doping ion concentration reduced the average particle size up to 9.81 ± 1.41 nm and 11.17 ± 0.83 nm, respectively. Alternatively, Sr^{2+} incorporation showed a higher influence on the particle size and morphology. For the samples obtained using eggshells as a CaO source, Sr incorporation decreased the average particle size to 9.03 ± 1.33 nm, while the samples obtained using mussel shells as a CaO source presented an average particle size of 9.53 ± 1.31 nm. Moreover, the higher concentration of Sr^{2+} further reduced the particle size. All these modifications in the particle size of the ion-substituted samples increased the tendency for particle agglomeration.

The consistency of the near-Gaussian distribution of different doping concentrations indicates a progressive reduction in particle size and distribution width. Further, the ion substituted into the HAp lattice proved to control nanoparticle formation and potentially disrupt crystal growth or induce lattice strains. All doped samples demonstrated a decrease in particle size by increasing ion concentration and creating more uniformly sized nanoparticles. This phenomenon is particularly highlighted for the Sr-doped samples, possessing a significant impact on particle size reduction compared to Cu-doped samples.

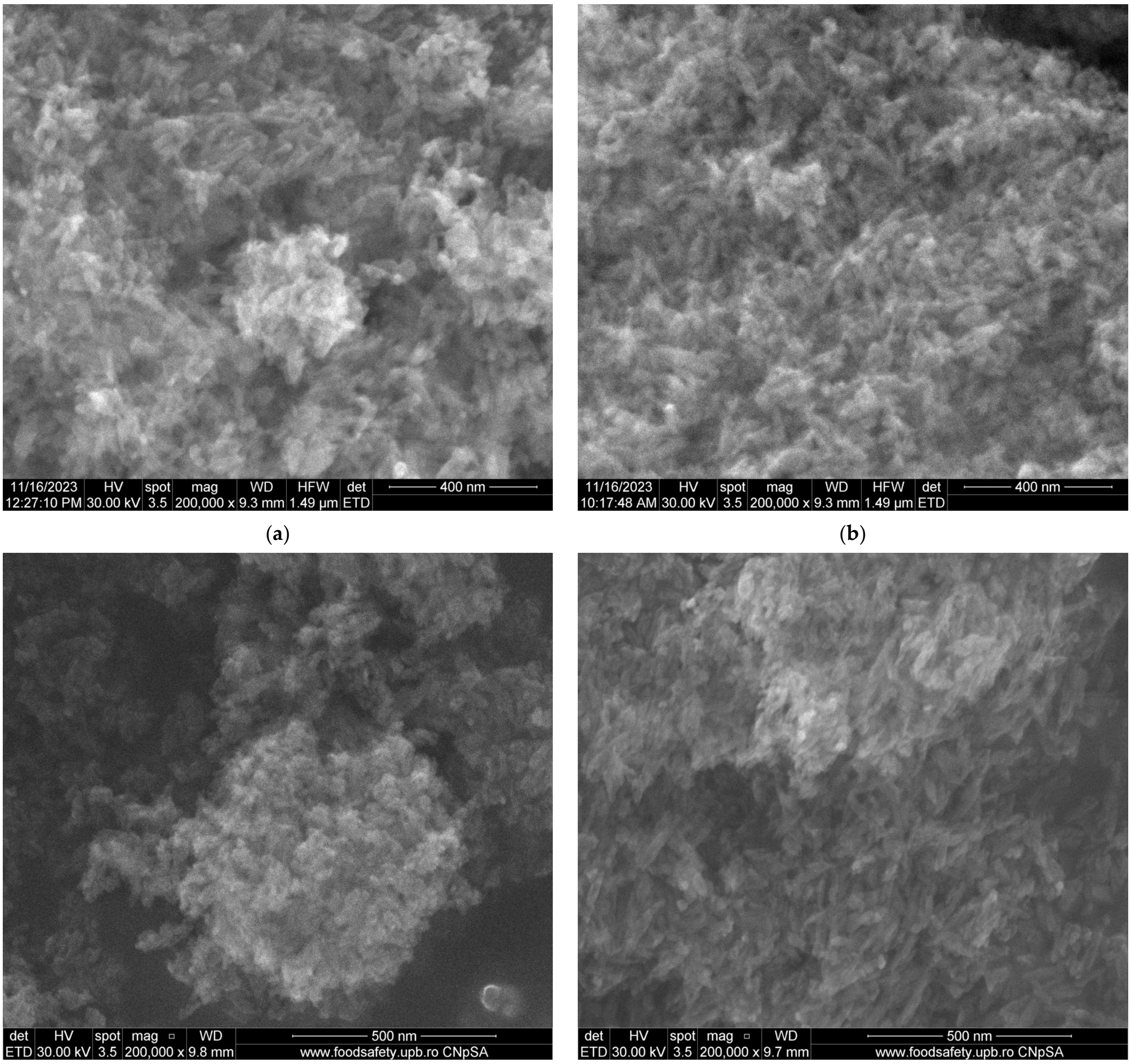

(**a**) (**b**) (**c**) (**d**)

Figure 3. *Cont.*

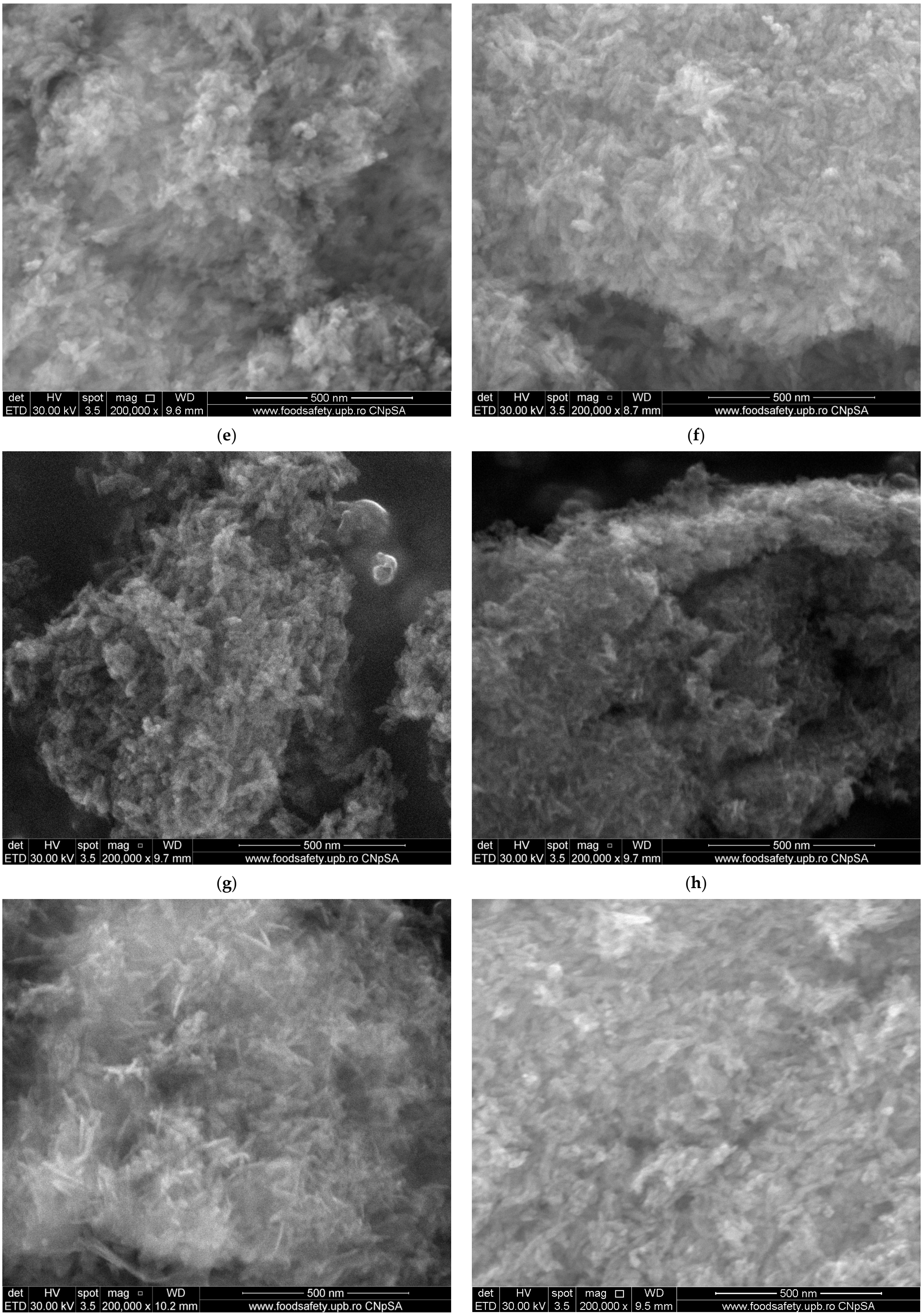

(**e**) (**f**)

(**g**) (**h**)

(**i**) (**j**)

Figure 3. SEM micrographs of the obtained samples: (**a**) HAp_C, (**b**) HAp_S, (**c**) HAp_Cu_1_C, (**d**) HAp_Cu_5_C, (**e**) HAp_Sr_1_C, (**f**) HAp_Sr_5_C, (**g**) HAp_Cu_1_S, (**h**) HAp_Cu_5_S, (**i**), HAp_Sr_1_S, (**j**) HAp_Sr_5_S.

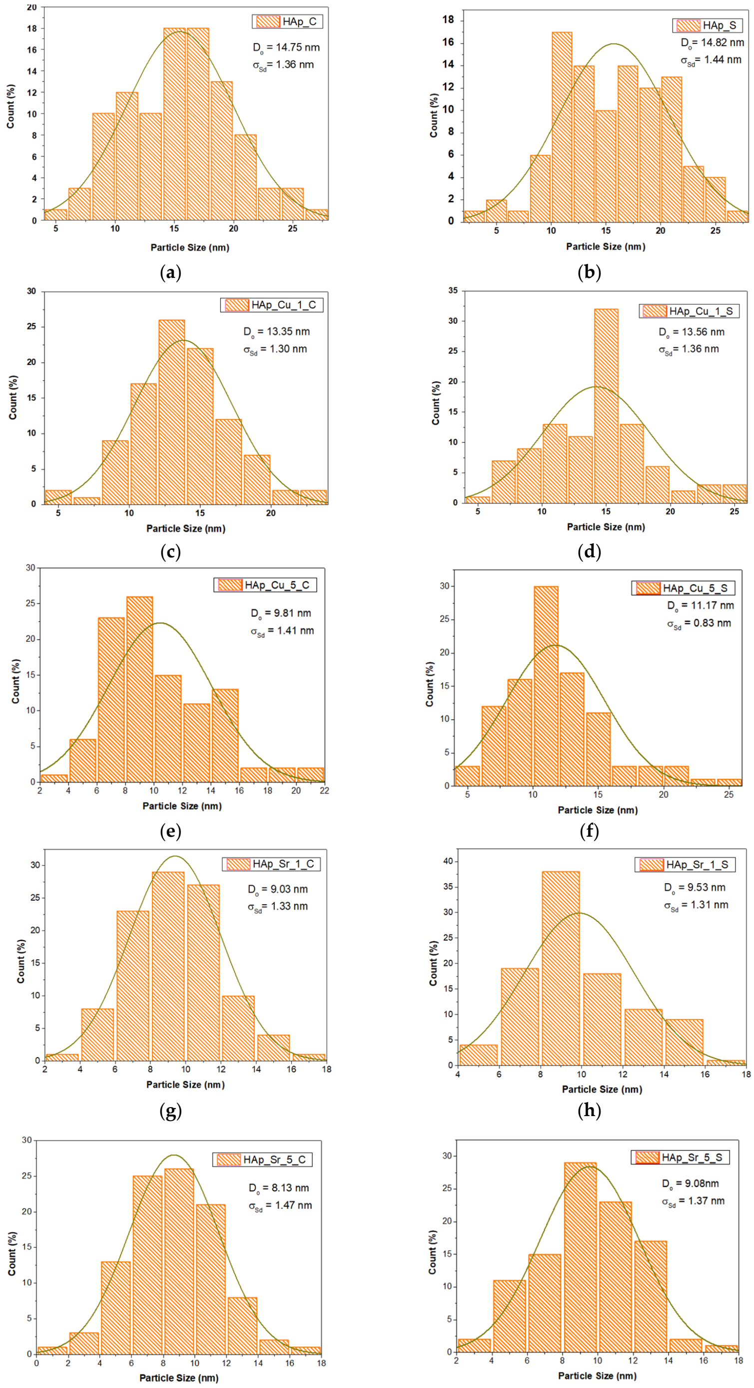

(**a**) (**b**)

(**c**) (**d**)

(**e**) (**f**)

(**g**) (**h**)

(**i**) (**j**)

Figure 4. The histogram of the particle size and average nanoparticle size of the obtained samples: (**a**) HAp_C, (**b**) HAp_S, (**c**) HAp_Cu_1_C, (**d**) HAp_Cu_1_S, (**e**) HAp_Cu_5_C, (**f**) HAp_Cu_5_S, (**g**) HAp_Sr_1_C, (**h**) HAp_Sr_1_S, (**i**), HAp_Sr_5_C, (**j**) HAp_Sr_5_S.

3.3. Transmission Electron Microscopy (TEM)

TEM analysis was conducted on 5% doped samples to evaluate nanoscale morphology and elemental distribution under maximum dopant loading. This concentration was selected as representing the maximum concentration of dopant incorporation while maintaining the structural integrity of the HAp lattice, as proven by XRD analysis. This concentration represents the optimal balance between significant morphological modification and maintained crystalline structure, providing the most pronounced nanoscale differences necessary for comprehensive structural characterization and elemental mapping analysis.

The TEM micrographs in Figure 5 show the nanoscale morphology and structural properties of both undoped and doped HAp samples. The undoped HAp samples have well-defined crystalline structures with rod-like and needle-like morphologies similar to HAp nanoparticles. For the 5% Cu^{2+} doping ion incorporation, the particles retain their elongated morphology but exhibit enhanced surface roughness and aggregation, with some particles having less uniform, faceted edges. The Sr^{2+}-doped samples show more pronounced morphological changes, including shorter, more compact rod-like structures with higher width-to-length ratios and increased inter-particle clustering. The doped samples demonstrate an increased agglomeration tendency and slightly altered particle morphologies compared to the undoped samples, with the production of bigger aggregated clusters.

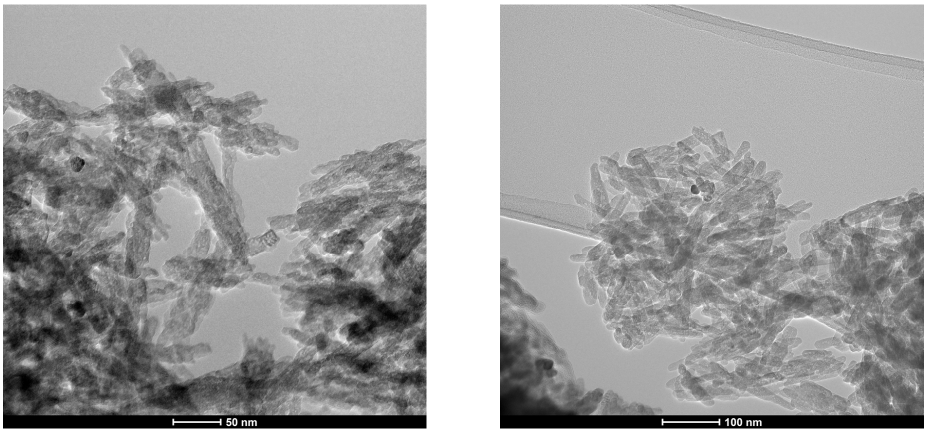

(**a**) HAp_C (**b**) HAp_S

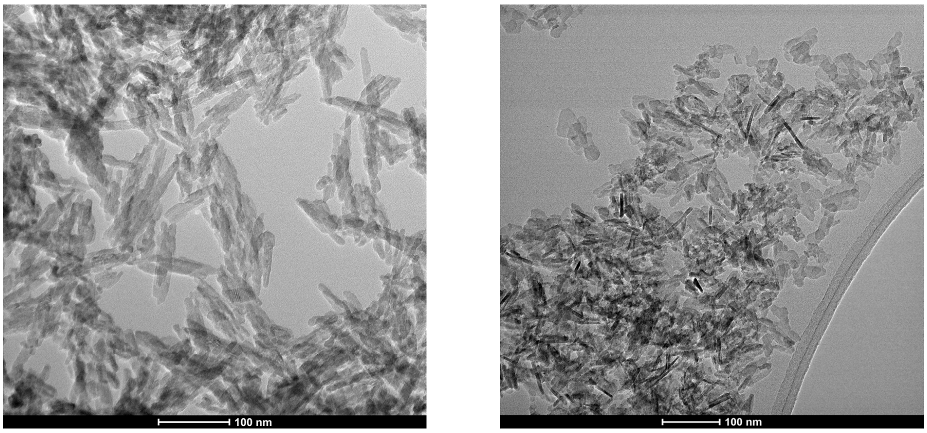

(**c**) HAp_Cu_5_C (**d**) HAp_Cu_5_S

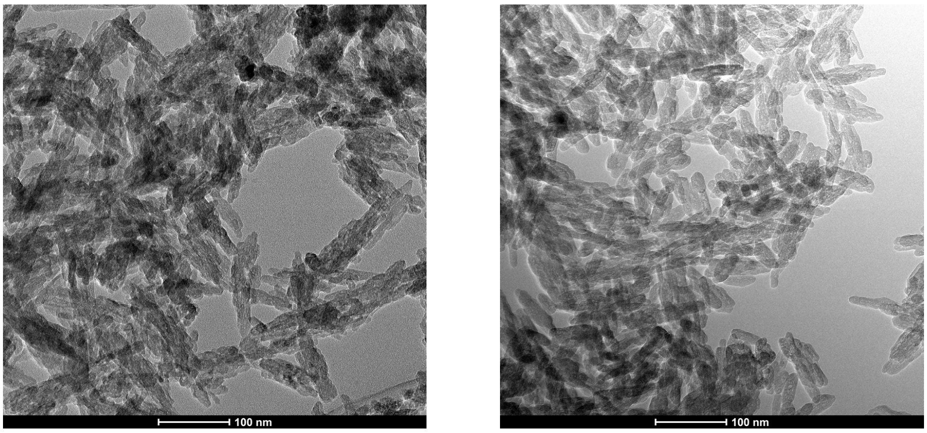

(**e**) HAp_Sr_5_C (**f**) HAp_Sr_5_S

Figure 5. TEM micrographs of the obtained samples: (**a**) HAp_C, (**b**) HAp_S, (**c**) HAp_Cu_5_C, (**d**) HAp_Cu_5_S, (**e**) HAp_Sr_5_C, (**f**) HAp_Sr_1_S.

The elemental mapping analysis (Figure 6) indicates that the dopant ions were successfully incorporated into the HAp structure. The mapping demonstrates a homogenous distribution of calcium (Ca), phosphorus (P), and oxygen (O) across all samples, as expected for the HAp matrix. The Cu trace in Cu-doped samples is equally distributed among the particles, indicating good substitution inside the crystal lattice. Similarly, the Sr distribution in the Sr-doped samples is uniform, indicating that Sr^{2+} ions were effectively incorporated into the HAp structure without phase separation.

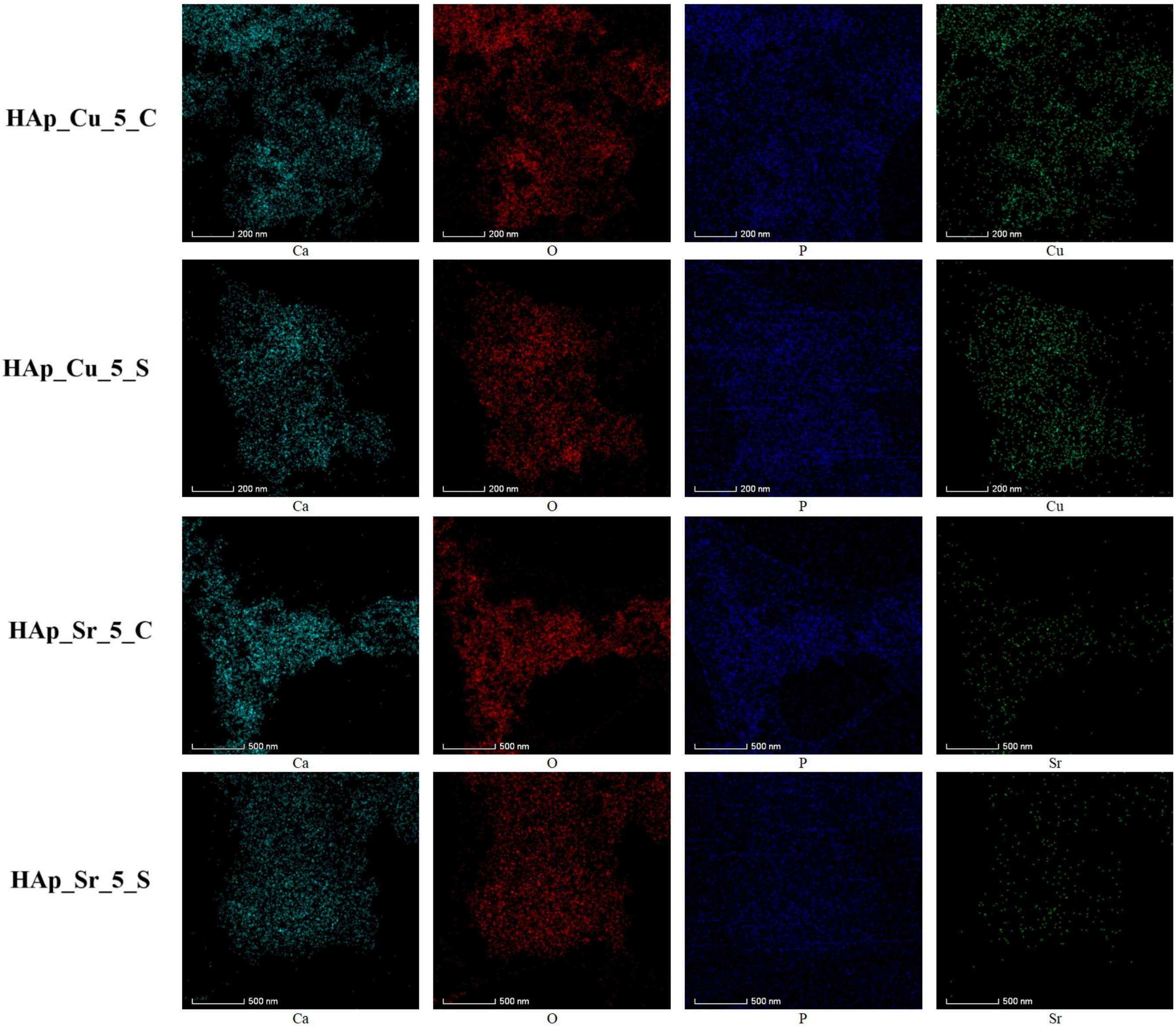

Figure 6. Elemental mapping of 5% Cu/Sr doped HAp samples.

Moreover, the TEM investigation confirms the XRD results, demonstrating that the doping technique preserves the overall structural integrity of HAp while introducing controlled compositional modifications. The mapping images show a consistent elemental distribution, which supports the conclusion that Cu^{2+} and Sr^{2+} ions are successfully incorporated into the HAp lattice rather than producing distinct phases.

3.4. Fourier-Transform Infrared Spectroscopy (FT-IR)

Fourier-transform infrared (FT-IR) spectra of undoped and doped HAp samples are presented in Figure 7. After investigating the materials obtained, the principal functional groups that correspond to HAp have been observed in all samples. According to the literature, the bands 590–600 cm^{-1} correspond to the υ1 symmetric stretching PO$_4^{3-}$, and 1018–1021 cm^{-1} correspond to the υ3 asymmetric stretching PO$_4^{3-}$ groups. Further, in all samples could be detected the υ2 vibration bands, but also the υ3 vibration bands of CO$_3^{2-}$ at 1413–1420 cm^{-1} and 1451–1537 cm^{-1}, respectively. Additionally, the broad peaks between 1640 and 1651 confirm the OH-bending vibrations, which are associated with the presence of the adsorbed water in the sample. Moreover, the stretching vibration of OH can also be identified around 3460–3500 cm^{-1}, specific for HAp [48,50].

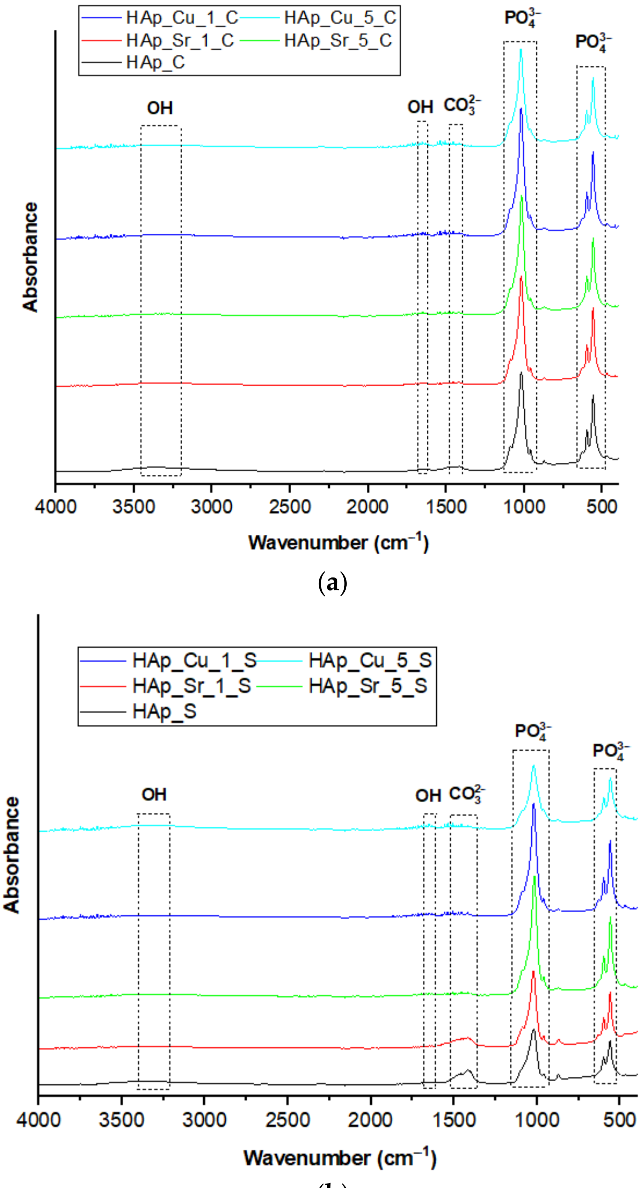

(**a**)

(**b**)

Figure 7. FT-IR spectrum of the doped samples compared to undoped HAp: (**a**) HAp obtained from eggshells, doped with 1% and 5% Cu and Sr, (**b**) HAp obtained from mussel shells, doped with 1% and 5% Cu and Sr.

All obtained materials presented the corresponding functional groups of HAp, while the incorporation of doping agents led to several modifications of the peaks. Considering Cu^{2+} or Sr^{2+} doping, ion substitution into the HAp lattice did not cause any modification of the functional groups; however, the intensity of OH groups decreased slightly with the doping of Sr or Cu. This is generated by the substitution of Ca^{2+} in the structure of HAp, confirming the results from XRD [49,51].

3.5. Inductively Coupled Plasma–Mass Spectrometry (ICP-MS)

Elemental analysis was performed to detect the trace elements found in the synthesized samples from their natural sources, mussel shells, and eggshells. As stated in Section 2.4.4, the amounts of Li, Be, Al, V, Co, Ni, Cr, Mn, Co, Ni, Zn, As, Cd, and Pb were also assessed. Moreover, this analysis confirms the success of Ca^{2+} substitutions with Cu^{2+} and Sr^{2+} ions. With the aid of ICP-MS, all HAp powders presented microelements, such as Sr, which are essential in the normal functions of the human body, especially in bone formation and regeneration. As shown in Table 4, it can be observed that all samples presented in their composition Sr. Further, it can also be observed that the substitution of Ca^{2+} with Cu^{2+} and Sr^{2+} occurs in the chemical composition of the developed samples.

Table 4. List of elements determined by ICP-MS for the obtained hydroxyapatite powders (1% and 5% represent the concentrations of the doping ions).

Sample	Cu	Sr
	(wt. %)	**(wt. %)**
HAp_C	n.d.	0.03
HAp_S	n.d.	0.08
HAp_Cu_1_C	0.76	0.03
HAp_Cu_1_S	0.77	0.10
HAp_Cu_5_C	3.29	0.03
HAp_Cu_5_S	3.58	0.09
HAp_Sr_1_C	n.d.	1.04
HAp_Sr_1_S	n.d.	1.23
HAp_Sr_5_C	n.d.	6.34
HAp_Sr_5_S	n.d.	5.48

n.d.: not detected.

Considering the natural source, mussel shells and eggshells used in the synthesis of HAp materials are known for their capacity to maintain specific trace elements, which lead to the enhancement of the biological activity of the obtained materials. In this regard, Sr is linked directly with the mineralization of calcified tissues, stimulating osteoblast proliferation and bone formation [52,53].

At the same time, Sr presents a higher significance in promoting bone regeneration, relating to the inhibition of osteoclast activity and stimulation of osteoblasts, which leads to new bone formation and decreased bone resorption. Moreover, researchers reported that Sr has a great influence on bone density, thus improving the bioactivity of the developed material [54,55]. As for the other metals, the concentrations were below the minimum limit of quantitation of 1 μg/L or undetectable even for the most concentrated stock sample solutions.

3.6. Biological Evaluation

Antimicrobial Analysis

Firstly, quantitative antimicrobial assessment involves establishing the MIC values, which are represented by the lowest concentration of the HAp samples that inhibits the growth of microbial strains. The MIC results are displayed in Figure 8 and are expressed as μg/μL.

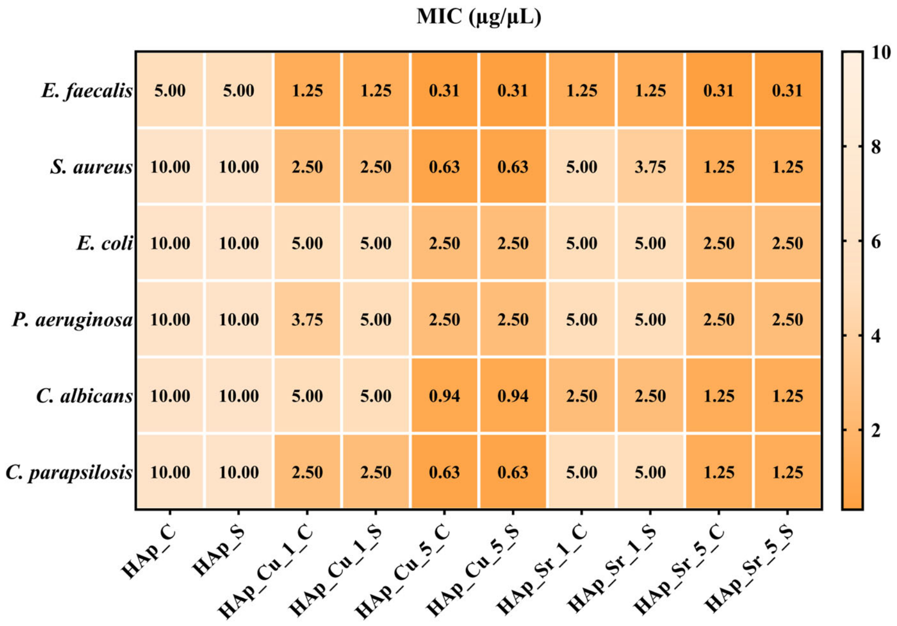

MIC (µg/µL)

	HAp_C	HAp_S	HAp_Cu_1_C	HAp_Cu_1_S	HAp_Cu_5_C	HAp_Cu_5_S	HAp_Sr_1_C	HAp_Sr_1_S	HAp_Sr_5_C	HAp_Sr_5_S
E. faecalis	5.00	5.00	1.25	1.25	0.31	0.31	1.25	1.25	0.31	0.31
S. aureus	10.00	10.00	2.50	2.50	0.63	0.63	5.00	3.75	1.25	1.25
E. coli	10.00	10.00	5.00	5.00	2.50	2.50	5.00	5.00	2.50	2.50
P. aeruginosa	10.00	10.00	3.75	5.00	2.50	2.50	5.00	5.00	2.50	2.50
C. albicans	10.00	10.00	5.00	5.00	0.94	0.94	2.50	2.50	1.25	1.25
C. parapsilosis	10.00	10.00	2.50	2.50	0.63	0.63	5.00	5.00	1.25	1.25

Figure 8. MIC values determined for HAp samples. The scale bar displays variations in the sensitivity of the strains from the highest (orange) to the lowest (light orange).

The lowest MIC values highlighted in Figure 8 represent the significant inhibitory effects of the HAp samples. The sensitivity of the strains is linked to the concentration of the doping agent (Cu and Sr), and the highest inhibitory effects are observed for HAp samples with 5% Cu. Moreover, the Gram-positive bacteria and *Candida* sp. tested strains are the most susceptible to the action of HAp samples.

Secondly, the MIC assay was followed by microbial adherence to the inert substratum analysis. The HAp samples' influence on the selected strains' adherence is shown in Figure 9 and represents the minimal biofilm eradication concentration (MBEC) values.

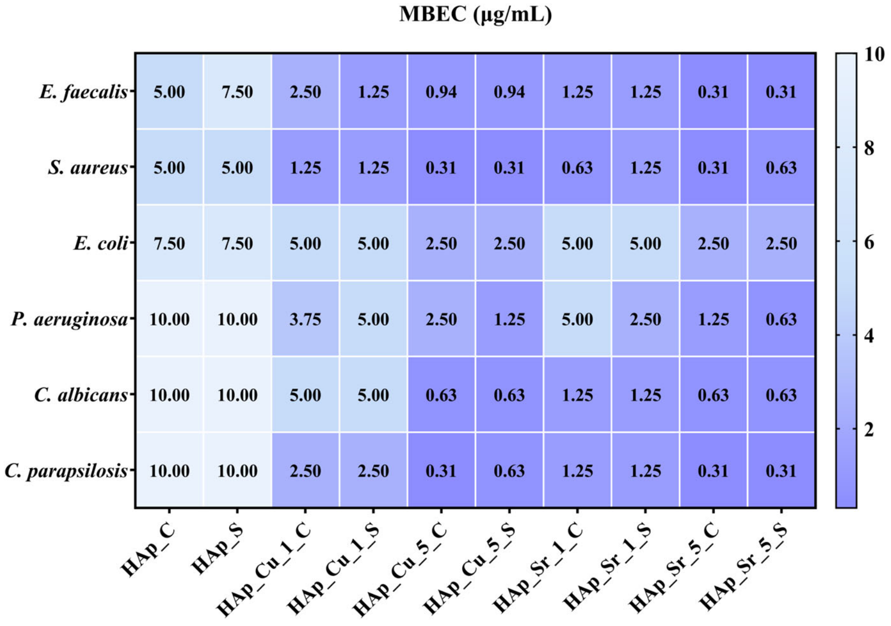

MBEC (µg/mL)

	HAp_C	HAp_S	HAp_Cu_1_C	HAp_Cu_1_S	HAp_Cu_5_C	HAp_Cu_5_S	HAp_Sr_1_C	HAp_Sr_1_S	HAp_Sr_5_C	HAp_Sr_5_S
E. faecalis	5.00	7.50	2.50	1.25	0.94	0.94	1.25	1.25	0.31	0.31
S. aureus	5.00	5.00	1.25	1.25	0.31	0.31	0.63	1.25	0.31	0.63
E. coli	7.50	7.50	5.00	5.00	2.50	2.50	5.00	5.00	2.50	2.50
P. aeruginosa	10.00	10.00	3.75	5.00	2.50	1.25	5.00	2.50	1.25	0.63
C. albicans	10.00	10.00	5.00	5.00	0.63	0.63	1.25	1.25	0.63	0.63
C. parapsilosis	10.00	10.00	2.50	2.50	0.31	0.63	1.25	1.25	0.31	0.31

Figure 9. MBEC values determined for HAp samples. The scale bar displays variations in the sensitivity of the strains from the highest (blue) to the lowest (light blue).

The MBEC values (Figure 9) confirm the MIC results (Figure 6), which are associated with the dosage of Cu and Sr. Consequently, *E. faecalis*, *S. aureus*, *C. parapsilosis*, and *C.*

albicans depicted the highest sensitivity in the presence of HAp-doped samples. The MBEC values ranged from 0.31 to 2.5 μg/μL for samples with 5% Cu or Sr. Also, significant antibiofilm effects were observed against Gram-negative bacterial strains. Our results indicated that the antimicrobial properties of the HAp samples are dose-dependent with Cu and Sr concentration, which follows previous studies [56–59].

Biocompatibility Assay

To investigate the biological activity of undoped and doped HAp samples, MC3T3-E1 osteoblast cells were used for the XTT assay. Duplicate experiments were performed for each sample, and the results of each obtained material are shown in Figure 10. After performing the in vitro experiments, only the samples containing 5% Sr presented a decreased cellular viability after 24 h. This decrease is influenced by the release of ion kinetics associated with increasing Sr concentrations. At 5% doping concentration, the initial burst release of Sr^{2+} ions may create a temporally increased ionic environment, causing osmotic stress and metabolic disturbance in osteoblast cells during this initial transition period [60,61]. These results are consistent with dose-dependent cellular responses, in which higher concentrations of bioactive ions require longer adjusting times for cells to achieve homeostatic balance [62].

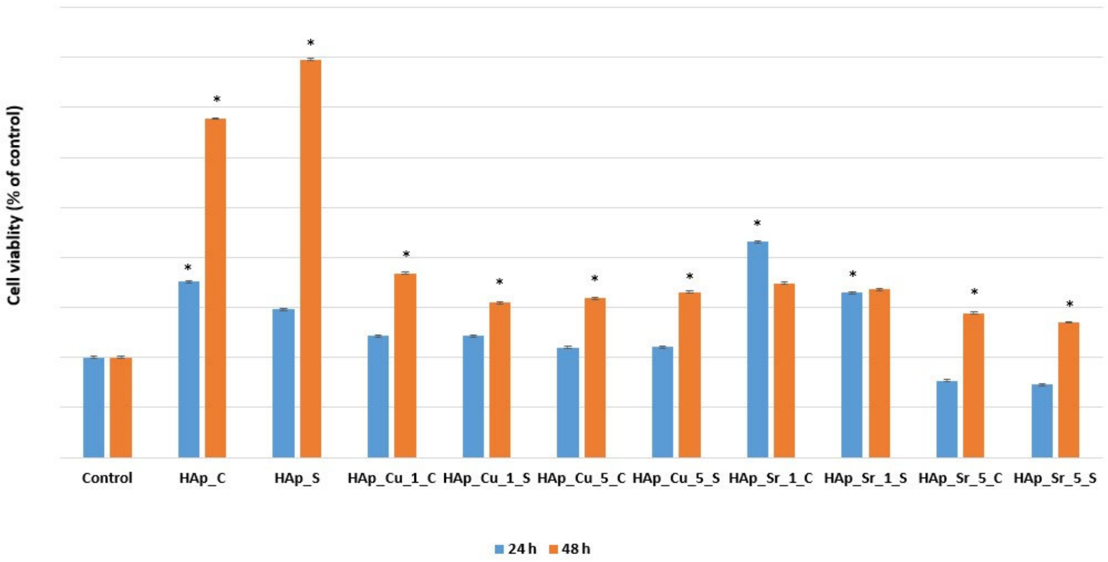

Figure 10. Cell viability results of undoped and doped HAp samples. The bars represent the standard deviations of the absorbances obtained, *—$p < 0.05$.

From Figure 10, the superior cellular viability for the eggshell and mussel shell-derived HAp could be observed, highlighting once again the importance of biomaterial origin. These results emphasized how the chemical compositions and structural characteristics of the developed samples influenced the material performance. At the same time, cell viability increased exponentially for almost all samples, as shown in Figure 10. The 1% Sr-doped samples showed statistically significant stable biocompatibility, representing a remarkable discovery. This observation not only aligns with the existing literature on strontium's role in bone metabolism but also provides good evidence of the doping dosage, which can potentially stimulate bone formation while minimizing adverse cellular responses.

Furthermore, Cu-doped samples demonstrated good potential for enhancing cellular response. The ANOVA analysis revealed not just simple variations, but statistically significant results that recommend them as important approaches as biomaterials for bone tissue engineering. Considering these results, all doped/undoped HAp materials proved their efficiency due to their capacity to be biocompatible substrates to support osteoblast cell proliferation. Additionally, doping ions are known for their beneficial activities in osseous regeneration. In this regard, Sr is known for its capacity to increase osteoblasts and decrease the quantity and activity of osteoclasts. Further, this doping ion is acknowledged for the enhancement of bone strength and mass, and at the same time, to inhibit bone resorption and improve bone formation [63]. Simultaneously, Cu ions are also recommended for their ability to promote osteogenic differentiation and enhance antibacterial activity without the appearance of toxic effects [64].

4. Discussion

The present study introduces a novel approach to synthesizing HAp by using and comparing two distinct biogenic sources—eggshells and mussel shells—as CaO precursors through a microwave-assisted hydrothermal treatment. While previous studies have explored these materials separately, this work uniquely demonstrates the comparative advantages of both sources with the same synthesis route, exploring their distinct impacts on the HAp properties. Additionally, this study further investigated the effects of Sr^{2+} and Cu^{2+} ion substitutions, providing new insights about how the CaO sources interact with dopants to influence crystallinity, morphology, and biological performance. This comprehensive approach not only expands our understanding of biogenic HAp synthesis but also establishes a sustainable and efficient pathway for developing tailored bioceramics with enhanced properties for specific biomedical applications.

Firstly, the successful synthesis of HAp was demonstrated using natural CaO sources derived from eggshells and mussel shells. This was confirmed by the diffraction patterns shown in Figure 1. The use of both precursors enabled the synthesis of HAp, with a small amount of $Ca(OH)_2$ detected as a secondary phase in the samples obtained by using eggshells as CaO precursors. Considering this, the microwave-assisted hydrothermal treatment successfully promoted the formation of HAp regardless of the CaO source. Both unsubstituted and substituted samples confirmed the desired crystal structure, as indicated by the diffraction patterns and corresponding ICDD specifications. Furthermore, the use of Sr^{2+} and Cu^{2+} ions could be observed from the slight modification in crystallinity [65]. While Sr^{2+} ions led to a slight increase in crystallinity, as observed by sharper diffraction peaks, Cu^{2+} substitution generated a reduction in crystallinity, as evidenced by a decrease in the intensity of the diffraction peaks. Begam [66] also reported a contraction of the lattice parameters, generated by the decrease of the unit cell volume, thus leading to a decrease in crystallinity. Nevertheless, studies such as the one performed by Huang et al. [67] confirmed that the incorporation of substitution ions leads to diffraction peaks shifting to the left. Additionally, the shift of diffraction peaks towards lower angles further supports these modifications, highlighting that the incorporation of dopants significantly influences the structural characteristics of HAp. Furthermore, ion substitution has also been confirmed from the Rietveld refinement analysis, as the unit cell parameters showed measurable changes. Specifically, Sr^{2+} substitution increased the lattice parameters, indicating its integration within the HAp lattice. On the other hand, Cu^{2+} ions have been demonstrated to fill interstitial positions rather than substituting directly for Ca^{2+}, given the substantial difference in ionic radii [68,69]. In this direction, Klinkla et al. [70] confirmed an increase in the cell volume due to the ionic atomic relaxation, which was also reported extensively in the literature.

The incorporation of substitute ions also shows a significant influence on the morphological properties of the nanoparticles. While substituting ion concentration increased, the tendency of nanoparticles to agglomerate also increased. Furthermore, the source used for CaO precursors also affected the size distribution. Pal et al. [71] and Sinulingga et al. [72] demonstrated that by increasing the doping ion concentration, the particle size distribution also decreased, which is also consistent with the results obtained in Figure 3. This size difference could be associated with the inherent characteristics of the natural precursors, as well as the influence of dopants on particle growth. Moreover, the influence of Sr^{2+} and Cu^{2+} substitution on crystallite size is a significant structural modification that influences the biological performance of the material. To support these findings, TEM analysis further confirmed these structural changes, showing that Cu^{2+}-doped samples had less uniform particle edges and increased surface roughness, which was in line with the reduced crystallinity shown in XRD patterns. Sr^{2+}-doped samples, on the other hand, demonstrated more compact morphologies while retaining structural integrity, confirming the successful lattice incorporation evidence provided by XRD.

According to our XRD study and Rietveld refinement results (Table 3), both dopants considerably altered crystallite size via separate methods. Sr^{2+} doping lowered the average crystallite size, whereas Cu^{2+} doping resulted in more complex crystallite sizes. The incorporation of Sr^{2+} reduces crystallite size due to structural distortions induced by lattice strain. This limits crystal development and promotes the formation of smaller crystallites. At the same time, Cu^{2+} doping alters the usual crystal lattice structure, creating strain fields that affect crystallite growth kinetics. These crystallite size modifications are essential for biomedical applications because smaller crystallites have a higher surface area, faster dissolution rates, and increased bioactivity, all of which can improve bone integration and remodeling processes.

Likewise, FT-IR analysis further confirmed the successful incorporation of Sr^{2+} and Cu^{2+} ions within the HAp lattice without modifying the primary functional groups associated with HAp. Oladipupo et al. [73] also confirmed the potential of using natural sources as CaO precursors to obtain HAp by identifying the main functional groups. The functional groups remained stable across all synthesized samples, confirming that ion substitution did not alter the chemical integrity of HAp. Moreover, the elemental analysis highlighted the presence of trace elements such as Mg and Sr. The eggshell-derived samples exhibited higher Mg content, while the mussel shell-derived HAp showed increased Sr content. This indicated that natural sources of CaO influence the final composition of the synthesized HAp, beneficial for potential biomedical applications. In this regard, Cestari et al. [74] also confirmed a similar presence of cations for the developed samples using eggshells (increased Mg^{2+} content) and mussel shells (increased Sr^{2+} content) as CaO precursor.

The development of multifunctional HAp materials with enhanced antibacterial characteristics has received a lot of interest as researchers become more concerned about implant-associated infections and antimicrobial resistance. Cu doping emerged as a promising strategy for increasing antimicrobial efficacy, with Cu ions exhibiting broad-spectrum activity through a variety of mechanisms, including membrane disruption, the generation of reactive oxygen species (ROS), and interference with essential protein and enzyme activities in microbial cells [75,76]. Furthermore, Sr ions offer an antimicrobial impact by modifying bacterial cell wall permeability and interfering with metabolic pathways, as demonstrated by their antibacterial activity against Bacillus subtilis and Pseudomonas aeruginosa strains [77]. The antimicrobial evaluation revealed significant dose-dependent activity, with 5% Cu-doped samples having the lowest MIC values of all tested bacteria. Cu^{2+} ions effectively disrupt cell membranes and generate reactive oxygen species, resulting in increased sensitivity in Gram-positive bacteria (*E. faecalis*, *S. aureus*) and Candida. The most effective compositions have MBEC values ranging from 0.31 to 2.5 μg/μL, indicating excellent biofilm removal potential. This addresses a critical barrier in implant-associated infections, as biofilms are extremely difficult to treat and often necessitate implant removal.

Related to the biological evaluation, MC3T3-E1 osteoblast cells were used to investigate the biocompatibility of the developed biomaterials. The obtained results proved that all synthesized HAp samples exhibited adequate biocompatibility. The decrease observed in cell viability for 5% Sr^{+}-doped samples at 24 h can be explained by various interconnected mechanisms associated with ion release kinetics and cellular adaptation. Studies demonstrated that fast Sr^{+} release increases ionic strength, leading to osmotic imbalances that can impact cell membrane integrity and intracellular water balance. Furthermore, the metabolic pathways responsible for Sr absorption into cellular functions may become saturated, resulting in transient metabolic stress and diminished viability after 24 h. This effect is a common dose-dependent response in which larger concentrations necessitate longer adaptation times for cells to achieve a new homeostatic equilibrium. Cell proliferation improves and rises over time in these samples, indicating that this is a transitory effect rather than constant cytotoxicity [78]. This understanding is critical for clinical translation, as it shows that 5% Sr^{2+} doping may require controlled release mechanisms to decrease initial cellular stress while maintaining long-term benefits of Sr absorption [61,79].

However, cell proliferation increased over time for all remaining samples, particularly those substituted with 1% Sr^{2+}, maintaining a consistent biocompatibility. In addition, Cu^{2+} substitution has also proven good potential for enhancing osteogenic differentiation, without inducing toxicity, suggesting its dual role in promoting bone regeneration and providing antibacterial activity. Alashi et al. [80] stated that ion incorporation promotes continuous ion release during the osseous remodeling process, enhancing the biological activity. Considering the use of biogenic sources, Li et al. [81] further confirmed that the presence of trace elements in biogenic sources can result in bioceramic materials similar to the mineral phase of natural osseous tissue, improving the osteogenic properties of the material and increasing the success rate of implantation.

5. Conclusions

In this work, undoped and Cu and Sr-doped HAp samples were synthesized through the co-precipitation synthesis method, followed by a microwave-assisted hydrothermal maturation process, while using biogenic sources as CaO precursors. The study has demonstrated successful synthesis of HAp through XRD analysis. Further, by performing the Rietveld refinement, the quantitative phase composition, structural parameters, and crystallinity were extracted to determine the influence of the dopant's concentration. All synthesized samples have been identified as HAp, with a hexagonal crystalline system. Ion substitution did not lead to any modifications of the crystal system, while the lattice parameters were modified. When speaking about the unit cell volume, their increasing values confirmed the incorporation of Cu^{2+} and Sr^{2+}. Regarding the morphological properties of the obtained samples, it could be observed that by increasing the doping concentration, the shape of the nanoparticles was modified, with a higher tendency to agglomerate. Furthermore, HAp obtained from mussel shells presents smaller nanoparticle dimensions compared to the ones obtained from eggshells.

Additionally, the HAp doping leads to modifications of sample crystallinity and crystallite size. With the aid of FT-IR analysis, the synthesis of HAp was once again confirmed by the corresponding functional groups. At the same time, ion substitution did not affect the bands of the main groups, while there was a slight decrease in their absorbance, which corresponded to the OH groups, generated by the substitution of Ca^{2+} in the structure of HAp. The presence of Cu^{2+} and Sr^{2+} was also proven by ICP-MS and elemental mapping, as well as the presence of trace elements from the mussel shells and eggshells. Furthermore, the biological evaluation demonstrated promising antibacterial and biocompatibility characteristics. Cu-doped samples presented good dose-dependent antimicrobial activity, with 5% Cu-doped HAp having the lowest MIC values (especially effective against Gram-positive bacteria and Candida species) and exceptional antibiofilm capabilities, with MBEC values ranging from 0.31 to 2.5 µg/µL. At the same time, biocompatibility testing on MC3T3-E1 osteoblast cells revealed that all samples maintained acceptable cell viability, with 1% Sr-doped samples exhibiting notably stable biocompatibility and Cu-doped samples improving cellular response. Shortly, more biological studies regarding osteogenesis should be performed to investigate its suitability and applicability in biomedical applications.

Author Contributions: Conceptualization, I.A.N.; Data curation, O.R.V., V.-A.S., A.C.B., G.D. and C.-I.I.; Formal analysis, O.R.V., V.-A.S., A.C.B. and C.-I.I.; Investigation, B.S.V., I.A.N., R.D.T., G.D. and C.-I.I.; Methodology, D.-E.R. and I.A.N.; Project administration, E.A.; Resources, B.S.V.; Supervision, E.A.; Visualization, D.-E.R. and R.D.T.; Writing—original draft, D.-E.R.; Writing—review and editing, B.S.V., I.A.N., D.-E.R. and E.A. All authors have read and agreed to the published version of the manuscript.

Funding: The work was supported by the project 'Activity-directed phosphate-ceramic scaffolds for regenerative bone tissue engineering' (no. 52/10.10.2023, grant ID: 220235125) granted by the National Program for Research of the National Association of Technical Universities-GNAC ARUT 2023.

Data Availability Statement: The original contributions presented in this study are included in the article. Further inquiries can be directed to the corresponding authors.

Acknowledgments: The authors are grateful to the Romanian Government for providing access to the research infra-structure of the National Center for Micro and Nanomaterials through the National Program titled "Installations and Strategic Objectives of National Interest".

Conflicts of Interest: The authors declare that they have no known competing financial interests or personal relationships that could have appeared to influence the work reported in this paper. Diana-Elena Radulescu is an employee of MDPI; however, they did not work for the Journal of Composites Science at the time of submission and publication.

References

1. Maleki-Ghaleh, H.; Siadati, M.H.; Fallah, A.; Zarrabi, A.; Afghah, F.; Koc, B.; Abdolahinia, E.D.; Omidi, Y.; Barar, J.; Akbari-Fakhrabadi, A.; et al. Effect of Zinc-Doped Hydroxyapatite/Graphene Nanocomposite on the Physicochemical Properties and Osteogenesis Differentiation of 3d-Printed Polycaprolactone Scaffolds for Bone Tissue Engineering. *Chem. Eng. J.* **2021**, *426*, 131321. [CrossRef]
2. Maleki-Ghaleh, H.; Siadati, M.H.; Fallah, A.; Koc, B.; Kavanlouei, M.; Khademi-Azandehi, P.; Moradpur-Tari, E.; Omidi, Y.; Barar, J.; Beygi-Khosrowshahi, Y.; et al. Antibacterial and Cellular Behaviors of Novel Zinc-Doped Hydroxyapatite/Graphene Nanocomposite for Bone Tissue Engineering. *Int. J. Mol. Sci.* **2021**, *22*, 9564. [CrossRef]
3. Shi, H.; Zhou, Z.; Li, W.; Fan, Y.; Li, Z.; Wei, J. Hydroxyapatite Based Materials for Bone Tissue Engineering: A Brief and Comprehensive Introduction. *Crystals* **2021**, *11*, 149. [CrossRef]
4. Osuchukwu, O.A.; Salihi, A.; Abdullahi, I.; Etinosa, P.O.; Obada, D.O. A Comparative Study of the Mechanical Properties of Sol-Gel Derived Hydroxyapatite Produced from a Novel Mixture of Two Natural Biowastes for Biomedical Applications. *Mater. Chem. Phys.* **2023**, *297*, 127434. [CrossRef]
5. Surya, P.; Nithin, A.; Sundaramanickam, A.; Sathish, M. Synthesis and Characterization of Nano-Hydroxyapatite from Sardinella Longiceps Fish Bone and Its Effects on Human Osteoblast Bone Cells. *J. Mech. Behav. Biomed. Mater.* **2021**, *119*, 104501. [CrossRef] [PubMed]
6. Firdaus Hussin, M.S.; Abdullah, H.Z.; Idris, M.I.; Abdul Wahap, M.A. Extraction of Natural Hydroxyapatite for Biomedical Applications—A Review. *Heliyon* **2022**, *8*, e10356. [CrossRef] [PubMed]
7. Cursaru, L.M.; Iota, M.; Piticescu, R.M.; Tarnita, D.; Savu, S.V.; Savu, I.D.; Dumitrescu, G.; Popescu, D.; Hertzog, R.-G.; Calin, M. Hydroxyapatite from Natural Sources for Medical Applications. *Materials* **2022**, *15*, 5091. [CrossRef] [PubMed]
8. Wu, S.-C.; Hsu, H.-C.; Wu, W.-H.; Ho, W.-F. Enhancing Bioactivity and Mechanical Properties of Nano-Hydroxyapatite Derived from Oyster Shells through Hydrothermal Synthesis. *Nanomaterials* **2024**, *14*, 1281. [CrossRef]
9. Pon-On, W.; Suntornsaratoon, P.; Charoenphandhu, N.; Thongbunchoo, J.; Krishnamra, N.; Tang, I.M. Hydroxyapatite from Fish Scale for Potential Use as Bone Scaffold or Regenerative Material. *Mater. Sci. Eng. C* **2016**, *62*, 183–189. [CrossRef]
10. Nam, P.V.; Hoa, N.V.; Trung, T.S. Properties of Hydroxyapatites Prepared from Different Fish Bones: A Comparative Study. *Ceram. Int.* **2019**, *45*, 20141–20147. [CrossRef]

11. Zubieta-Otero, L.F.; Gomez-Vazquez, O.M.; Correa-Piña, B.A.; Rodriguez-Garcia, M.E. Bio-Inspired Synthesis of Bio-Hydroxyapatite/Synthetic Hydroxyapatite Hybrid Nanosystems. *MedComm—Biomater. Appl.* **2023**, *2*, e64. [CrossRef]
12. Alturki, A.M.; Abu-Rayyan, A.; Abualnaja, K.M.; Alhashmialameer, D.; El-Saeed, R.A.; El-Shabasy, R.M. Physicomechanical and Morphological Properties of Hydroxyapatite Nanocrystals Substituted with Copper–Zirconium. *J. Mater. Res. Technol.* **2021**, *14*, 2312–2321. [CrossRef]
13. Noviyanti, A.R.; Rahayu, I.; Fauzia, R.P.; Risdiana. The Effect of Mg Concentration to Mechanical Strength of Hydroxyapatite Derived from Eggshell. *Arab. J. Chem.* **2021**, *14*, 103032. [CrossRef]
14. Bootchanont, A.; Wechprasit, T.; Areesamarn, N.; Pholprom, R.; Hwangphon, T.; Temprom, L.; Amonpattaratkit, P.; Klysubun, W.; Yimnirun, R. Comparison of Local Structure between Mg/Mn-Doped Natural and Synthetic Hydroxyapatites by X-Ray Absorption Spectroscopy. *Radiat. Phys. Chem.* **2020**, *177*, 109075. [CrossRef]
15. Sivakumar, P.M.; Yetisgin, A.A.; Sahin, S.B.; Demir, E.; Cetinel, S. Enhanced Properties of Nickel–Silver Codoped Hydroxyapatite for Bone Tissue Engineering: Synthesis, Characterization, and Biocompatibility Evaluation. *Environ. Res.* **2023**, *238*, 117131. [CrossRef]
16. Radulescu, D.-E.; Vasile, O.R.; Andronescu, E.; Ficai, A. Latest Research of Doped Hydroxyapatite for Bone Tissue Engineering. *Int. J. Mol. Sci.* **2023**, *24*, 13157. [CrossRef]
17. Uskoković, V. Ion-Doped Hydroxyapatite: An Impasse or the Road to Follow? *Ceram. Int.* **2020**, *46*, 11443–11465. [CrossRef]
18. Murugesan, V.; Vaiyapuri, M.; Murugeasan, A. Fabrication and Characterization of Strontium Substituted Chitosan Modify Hydroxyapatite for Biomedical Applications. *Inorg. Chem. Commun.* **2022**, *142*, 109653. [CrossRef]
19. Nenen, A.; Maureira, M.; Neira, M.; Orellana, S.L.; Covarrubias, C.; Moreno-Villoslada, I. Synthesis of Antibacterial Silver and Zinc Doped Nano-Hydroxyapatite with Potential in Bone Tissue Engineering Applications. *Ceram. Int.* **2022**, *48*, 34750–34759. [CrossRef]
20. Jiang, X.; Zhao, Y.; Wang, C.; Sun, R.; Tang, Y. Effects of Physico-Chemical Properties of Ions-Doped Hydroxyapatite on Adsorption and Release Performance of Doxorubicin as a Model Anticancer Drug. *Mater. Chem. Phys.* **2022**, *276*, 125440. [CrossRef]
21. Matić, T.; Zebić, M.L.; Miletić, V.; Cvijović-Alagić, I.; Petrović, R.; Janaćković, D.; Veljović, D. Sr,Mg Co-Doping of Calcium Hydroxyapatite: Hydrothermal Synthesis, Processing, Characterization and Possible Application as Dentin Substitutes. *Ceram. Int.* **2022**, *48*, 11155–11165. [CrossRef]
22. Dorcioman, G.; Grumezescu, V.; Stan, G.E.; Chifiriuc, M.C.; Gradisteanu, G.P.; Miculescu, F.; Matei, E.; Popescu-Pelin, G.; Zgura, I.; Craciun, V.; et al. Hydroxyapatite Thin Films of Marine Origin as Sustainable Candidates for Dental Implants. *Pharmaceutics* **2023**, *15*, 1294. [CrossRef] [PubMed]
23. Singh, R.P.; Singh, J.P.; Pal, A.; Kaur, T. Encapsulation of Vancomycin in Copper Doped Hydroxyapatite Mesoporous Nanoparticles of Different Morphologies. *J. Drug Deliv. Sci. Technol.* **2020**, *55*, 101441. [CrossRef]
24. Megha, M.; Joy, A.; Unnikrishnan, G.; Haris, M.; Thomas, J.; Deepti, A.; Chakrapani, P.S.B.; Kolanthai, E.; Muthuswamy, S. Structural and Biological Properties of Novel Vanadium and Strontium Co-Doped Hap for Tissue Engineering Applications. *Ceram. Int.* **2023**, *49*, 30156–30169. [CrossRef]
25. Abdalla, M.M.; Sayed, O.; Lung, C.Y.K.; Rajasekar, V.; Yiu, C.K.Y. Applications of Bioactive Strontium Compounds in Dentistry. *J. Funct. Biomater.* **2024**, *15*, 216. [CrossRef]
26. Yuan, Q.; Zhang, Z.; Yang, Y.; Jian, Y.; Li, R.; Dai, X.; Wu, W.; Zhong, J.; Chen, C. Synthesis, Characterization and Biological Performance Study of Sr-Doped Hydroxyapatite/Chitosan Composite Coatings. *Mater. Chem. Phys.* **2021**, *270*, 124752. [CrossRef]
27. Zhu, H.; Guo, D.; Sun, L.; Li, H.; Hanaor, D.A.; Schmidt, F.; Xu, K. Nanostructural Insights into the Dissolution Behavior of Sr-Doped Hydroxyapatite. *J. Eur. Ceram. Soc.* **2018**, *38*, 5554–5562. [CrossRef]
28. Veljovic, D.; Matic, T.; Stamenic, T.; Kojic, V.; Dimitrijevic-Brankovic, S.; Lukic, M.J.; Jevtic, S.; Radovanovic, Z.; Petrovic, R.; Janackovic, D. Mg/Cu Co-Substituted Hydroxyapatite—Biocompatibility, Mechanical Properties and Antimicrobial Activity. *Ceram. Int.* **2019**, *45*, 22029–22039. [CrossRef]
29. Jacobs, A.; Renaudin, G.; Charbonnel, N.; Nedelec, J.-M.; Forestier, C.; Descamps, S. Copper-Doped Biphasic Calcium Phosphate Powders: Dopant Release, Cytotoxicity and Antibacterial Properties. *Materials* **2021**, *14*, 2393. [CrossRef]
30. Bulina, N.V.; Eremina, N.V.; Vinokurova, O.B.; Ishchenko, A.V.; Chaikina, M.V. Diffusion of Copper Ions in the Lattice of Substituted Hydroxyapatite During Heat Treatment. *Materials* **2022**, *15*, 5759. [CrossRef]
31. Burdusel, A.-C.; Neacsu, I.A.; Birca, A.C.; Chircov, C.; Grumezescu, A.-M.; Holban, A.M.; Curutiu, C.; Ditu, L.M.; Stan, M. Microwave-Assisted Hydrothermal Treatment of Multifunctional Substituted Hydroxyapatite with Prospective Applications in Bone Regeneration. *J. Funct. Biomater.* **2023**, *14*, 378. [CrossRef] [PubMed]
32. Dumitrescu, C.R.; Neacsu, I.A.; Surdu, V.A.; Nicoara, A.I.; Iordache, F.; Trusca, R.; Ciocan, L.T.; Ficai, A.; Andronescu, E. Nano-Hydroxyapatite Vs. Xenografts: Synthesis, Characterization, and in Vitro Behavio. *Nanomaterials* **2021**, *11*, 2289. [CrossRef] [PubMed]
33. Chen, J.; Liu, J.; Deng, H.; Yao, S.; Wang, Y. Regulatory Synthesis and Characterization of Hydroxyapatite Nanocrystals by a Microwave-Assisted Hydrothermal Method. *Ceram. Int.* **2020**, *46*, 2185–2193. [CrossRef]

34. Karunakaran, G.; Kumar, G.S.; Cho, E.-B.; Sunwoo, Y.; Kolesnikov, E.; Kuznetsov, D. Microwave-Assisted Hydrothermal Synthesis of Mesoporous Carbonated Hydroxyapatite with Tunable Nanoscale Characteristics for Biomedical Applications. *Ceram. Int.* **2019**, *45*, 970–977. [CrossRef]
35. Méndez-Lozano, N.; Velázquez-Castillo, R.; Rivera-Muñoz, E.M.; Bucio-Galindo, L.; Mondragón-Galicia, G.; Manzano-Ramírez, A.; Ocampo, M.Á.; Apátiga-Castro, L.M. Crystal Growth and Structural Analysis of Hydroxyapatite Nanofibers Synthesized by the Hydrothermal Microwave-Assisted Method. *Ceram. Int.* **2017**, *43*, 451–457. [CrossRef]
36. Patil, H.G.; Rajendran, A.; Lenka, N.; Kumar, B.S.; Murugesan, S.; Anandhan, S. Probing the Influence of Strontium Doping and Annealing Temperature on the Structure and Biocompatibility of Hydroxyapatite Nanorods. *Dalton Trans.* **2024**, *53*, 7812–7827. [CrossRef]
37. Aina, V.; Bergandi, L.; Lusvardi, G.; Malavasi, G.; Imrie, F.E.; Gibson, I.R.; Cerrato, G.; Ghigo, D. Sr-Containing Hydroxyapatite: Morphologies of Ha Crystals and Bioactivity on Osteoblast Cells. *Mater. Sci. Eng. C* **2013**, *33*, 1132–1142. [CrossRef]
38. Tite, T.; Popa, A.-C.; Balescu, L.M.; Bogdan, I.M.; Pasuk, I.; Ferreira, J.M.F.; Stan, G.E. Cationic Substitutions in Hydroxyapatite: Current Status of the Derived Biofunctional Effects and Their in Vitro Interrogation Methods. *Materials* **2018**, *11*, 2081. [CrossRef]
39. Baldassarre, F.; Altomare, A.; Mesto, E.; Lacalamita, M.; Dida, B.; Mele, A.; Bauer, E.M.; Puzone, M.; Tempesta, E.; Capelli, D.; et al. Structural Characterization of Low-Sr-Doped Hydroxyapatite Obtained by Solid-State Synthesis. *Crystals* **2023**, *13*, 117. [CrossRef]
40. Ciobanu, C.S.; Predoi, D.; Iconaru, S.L.; Predoi, M.V.; Ghegoiu, L.; Buton, N.; Motelica-Heino, M. Copper Doped Hydroxyapatite Nanocomposite Thin Films: Synthesis, Physico–Chemical and Biological Evaluation. *BioMetals* **2024**, *37*, 1487–1500. [CrossRef]
41. Tuntun, S.M.; Sahadat Hossain, M.; Uddin, M.N.; Shaikh, M.A.A.; Bahadur, N.M.; Ahmed, S. Crystallographic Characterization and Application of Copper Doped Hydroxyapatite as a Biomaterial. *New J. Chem.* **2023**, *47*, 2874–2885. [CrossRef]
42. Anand, A.; Sengupta, S.; Galusek, D.; Beltrán, A.M.; Galusková, D.; Boccaccini, A.R. A New Approach to Overcome Cytotoxic Effects of Cu by Delivering Dual Therapeutic Ions (Sr, Cu). *J. Trace Elem. Med. Biol.* **2025**, *87*, 127565. [CrossRef]
43. Al-Hammadi, A.H.; Al-Adhreai, A.a.A.; Abdulwahab, A.M.; Al-Adhreai, A.; Salem, A.; Alaizeri, Z.M.; Alsaeedy, M.; Katib Alanazi, F. An Investigation on the Structural, Morphological, Optical, and Antibacterial Activity of Sr:Cus Nanostructures. *Sci. Rep.* **2024**, *14*, 25169. [CrossRef]
44. Ilie, C.-I.; Spoiala, A.; Chircov, C.; Dolete, G.; Oprea, O.-C.; Vasile, B.-S.; Crainiceanu, S.A.; Nicoara, A.-I.; Marinas, I.C.; Stan, M.S.; et al. Antioxidant, Antitumoral, Antimicrobial, and Prebiotic Activity of Magnetite Nanoparticles Loaded with Bee Pollen/Bee Bread Extracts and 5-Fluorouracil. *Antioxidants* **2024**, *13*, 895. [CrossRef]
45. *CLSI M100*; Performance Standards for Antimicrobial Susceptibility Testing—35th Edition. Clinical and Laboratory Standards Institute: Wayne, PA, USA, 2025.
46. Obada, D.O.; Salami, K.A.; Oyedeji, A.N.; Fasanya, O.O.; Suleiman, M.U.; Ibisola, B.A.; Atta, A.Y.; Dodoo-Arhin, D.; Kuburi, L.S.; Dauda, M.; et al. Solution Combustion Synthesis of Strontium-Doped Hydroxyapatite: Effect of Sintering and Low Compaction Pressure on the Mechanical Properties and Physiological Stability. *Mater. Lett.* **2021**, *304*, 130613. [CrossRef]
47. Poovendran, K.; Wilson, K.S.J.; Revathy, M.S.; Ayeshamariam, A.; Kaviyarasu, K. Functionalization Effect of Hap with Copper (Cu) Having Excellent Dielectric Applications. *Surf. Interfaces* **2020**, *19*, 100474. [CrossRef]
48. Chadha, R.K.; Singh, K.L.; Sharma, C.; Singh, A.P.; Naithani, V. Effect of Microwave and Conventional Processing Techniques on Mechanical Properties of Strontium Substituted Hydroxyapatite. *Ceram. Int.* **2020**, *46*, 1091–1098. [CrossRef]
49. Unabia, R.B.; Bonebeau, S.; Candidato, R.T.; Jouin, J.; Noguera, O.; Pawłowski, L. Investigation on the Structural and Microstructural Properties of Copper-Doped Hydroxyapatite Coatings Deposited Using Solution Precursor Plasma Spraying. *J. Eur. Ceram. Soc.* **2019**, *39*, 4255–4263. [CrossRef]
50. Wang, B.; Li, Y.; Wang, S.; Jia, F.; Bian, A.; Wang, K.; Xie, L.; Yan, K.; Qiao, H.; Lin, H.; et al. Electrodeposited Dopamine/Strontium-Doped Hydroxyapatite Composite Coating on Pure Zinc for Anti-Corrosion, Antimicrobial and Osteogenesis. *Mater. Sci. Eng. C* **2021**, *129*, 112387. [CrossRef]
51. Li, K.; Li, S.; Ai, F.; Yan, J.; Zhou, K. Fabrication and Characterization of Sr-Doped Hydroxyapatite Porous Scaffold. *JOM* **2021**, *73*, 1745–1753. [CrossRef]
52. Shavandi, A.; Wilton, V.; Bekhit, A.E.-D.A. Synthesis of Macro and Micro Porous Hydroxyapatite (Ha) Structure from Waste Kina (Evechinus Chloroticus) Shells. *J. Taiwan Inst. Chem. Eng.* **2016**, *65*, 437–443. [CrossRef]
53. Ma, Q.; Rubenis, K.; Sigurjónsson, Ó.E.; Hildebrand, T.; Standal, T.; Zemjane, S.; Locs, J.; Loca, D.; Haugen, H.J. Eggshell-Derived Amorphous Calcium Phosphate: Synthesis, Characterization and Bio-Functions as Bone Graft Materials in Novel 3d Osteoblastic Spheroids Model. *Smart Mater. Med.* **2023**, *4*, 522–537. [CrossRef]
54. Sasireka, A.; Renji, R.; Mohan Raj, R.; Vignesh, S.; Raj, V.; Ashraf, I.M.; Shkir, M. Exploration on in Vitro Bioactivity, Antibacterial Activity and Corrosion Behavior of Strontium Doped Hydroxyapatite Reinforced Chitosan-Polypyrrole/Tnt for Bone Regeneration. *Inorg. Chem. Commun.* **2022**, *142*, 109621. [CrossRef]
55. Chen, T.; Wu, X.; Zhang, P.; Wu, W.; Dai, H.; Chen, S. Strontium-Doped Hydroxyapatite Coating Improves Osteo/Angiogenesis for Ameliorative Graft-Bone Integration Via the Macrophage-Derived Cytokines-Mediated Integrin Signal Pathway. *ACS Appl. Mater. Interfaces* **2024**, *16*, 15687–15700. [CrossRef] [PubMed]

56. Pham, D.Q.; Gangadoo, S.; Lu, Z.; Berndt, C.C.; Newsom, E.T.; Zreiqat, H.; Truong, V.K.; Ang, A.S.M. Strontium-Doped Hardystonite Plasma Sprayed Coatings with Robust Antimicrobial Activity. *Mater. Today Chem.* **2022**, *24*, 100822. [CrossRef]
57. Jamarun, N.; Afriska, L.N.; Wellia, D.V.; Prasejati, A.; Amirullah, T.Y.; Wulandari, W.; Trycahyani, N.A. *Investigation of the Antibacterial Activity of Synthesized Hydroxyapatite Sr-Doped Nanocomposite*; JAPS: Gwalior, India, 2024; Volume 14, pp. 264–269.
58. Hassanain, M.; Abdel-Ghafar, H.M.; Hamouda, H.I.; El-Hosiny, F.I.; Ewais, E.M.M. Enhanced Antimicrobial Efficacy of Hydroxyapatite-Based Composites for Healthcare Applications. *Sci. Rep.* **2024**, *14*, 26426. [CrossRef]
59. Noori, A.; Hoseinpour, M.; Kolivand, S.; Lotfibakhshaiesh, N.; Ebrahimi-Barough, S.; Ai, J.; Azami, M. Exploring the Various Effects of Cu Doping in Hydroxyapatite Nanoparticle. *Sci. Rep.* **2024**, *14*, 3421. [CrossRef]
60. Prabha, R.D.; Ding, M.; Bollen, P.; Ditzel, N.; Varma, H.K.; Nair, P.D.; Kassem, M. Strontium Ion Reinforced Bioceramic Scaffold for Load Bearing Bone Regeneration. *Mater. Sci. Eng. C* **2020**, *109*, 110427. [CrossRef]
61. Sheng, X.; Li, C.; Wang, Z.; Xu, Y.; Sun, Y.; Zhang, W.; Liu, H.; Wang, J. Advanced Applications of Strontium-Containing Biomaterials in Bone Tissue Engineering. *Mater. Today Bio* **2023**, *20*, 100636. [CrossRef]
62. Zhang, Y.; Liu, L.; Li, M.; Wang, S.; Fu, J.; Yang, M.; Yan, C.; Liu, Y.; Zheng, Y. Dose-Dependent Enhancement of in Vitro Osteogenic Activity on Strontium-Decorated Polyetheretherketone. *Sci. Rep.* **2025**, *15*, 3063. [CrossRef]
63. Capuccini, C.; Torricelli, P.; Boanini, E.; Gazzano, M.; Giardino, R.; Bigi, A. Interaction of Sr-Doped Hydroxyapatite Nanocrystals with Osteoclast and Osteoblast-Like Cells. *J. Biomed. Mater. Res. Part A* **2009**, *89*, 594–600. [CrossRef]
64. Shi, F.; Liu, Y.; Zhi, W.; Xiao, D.; Li, H.; Duan, K.; Qu, S.; Weng, J. The Synergistic Effect of Micro/Nano-Structured and Cu2+-Doped Hydroxyapatite Particles to Promote Osteoblast Viability and Antibacterial Activity. *Biomed. Mater.* **2017**, *12*, 035006. [CrossRef] [PubMed]
65. Geng, Z.; Cheng, Y.; Ma, L.; Li, Z.; Cui, Z.; Zhu, S.; Liang, Y.; Liu, Y.; Bao, H.; Li, X.; et al. Nanosized Strontium Substituted Hydroxyapatite Prepared from Egg Shell for Enhanced Biological Properties. *J. Biomater. Appl.* **2018**, *32*, 896–905. [CrossRef] [PubMed]
66. Begam, H.; Kundu, B.; Chanda, A.; Nandi, S.K. Mg63 Osteoblast Cell Response on Zn Doped Hydroxyapatite (Hap) with Various Surface Features. *Ceram. Int.* **2017**, *43*, 3752–3760. [CrossRef]
67. Huang, H.; Qiang, L.; Fan, M.; Liu, Y.; Yang, A.; Chang, D.; Li, J.; Sun, T.; Wang, Y.; Guo, R.; et al. 3d-Printed Tri-Element-Doped Hydroxyapatite/Polycaprolactone Composite Scaffolds with Antibacterial Potential for Osteosarcoma Therapy and Bone Regeneration. *Bioact. Mater.* **2024**, *31*, 18–37. [CrossRef]
68. Terra, J.; Dourado, E.R.; Eon, J.-G.; Ellis, D.E.; Gonzalez, G.; Rossi, A.M. The Structure of Strontium-Doped Hydroxyapatite: An Experimental and Theoretical Study. *Phys. Chem. Chem. Phys.* **2009**, *11*, 568–577. [CrossRef]
69. Kawabata, K.; Yamamoto, T. First-Principles Calculations of the Elastic Properties of Hydroxyapatite Doped with Divalent Ions. *J. Ceram. Soc. Jpn.* **2010**, *118*, 548–549. [CrossRef]
70. Klinkla, R.; Kaewmaraya, T.; Bootchanon, A.; Saisopa, T.; Fongkaew, I.; Yimnirun, R.; Khamkongkaeo, A.; Rattanachai, Y.; Sailuam, W. Effects of Sr and Mg Doping on Elastic, Mechanical, and Optical Properties of Hydroxyapatite: A First-Principles Study. *Results Phys.* **2024**, *57*, 107352. [CrossRef]
71. Pal, A.; Nasker, P.; Paul, S.; Roy Chowdhury, A.; Sinha, A.; Das, M. Strontium Doped Hydroxyapatite from Mercenaria Clam Shells: Synthesis, Mechanical and Bioactivity Study. *J. Mech. Behav. Biomed. Mater.* **2019**, *90*, 328–336. [CrossRef]
72. Sinulingga, K.; Sirait, M.; Siregar, N.; Abdullah, H. Synthesis and Characterizations of Natural Limestone-Derived Nano-Hydroxyapatite (Hap): A Comparison Study of Different Metals Doped Haps on Antibacterial Activity. *RSC Adv.* **2021**, *11*, 15896–15904. [CrossRef]
73. Oladipupo, O.F.; Adekola, A.H.; Ofudje, E.A.; Al-Ahmary, K.M.; Al-Mhyawi, S.R.; Alshdoukhi, I.F.; Alrahili, M.R.; Alsaiari, A.A. Eggshell Derived Scaffold of Hydroxyapatite-Ammonium Bicarbonate Nano-Composite: Bioactivity and Cytotoxicity Studies. *Heliyon* **2024**, *10*, e36493. [CrossRef] [PubMed]
74. Cestari, F.; Agostinacchio, F.; Galotta, A.; Chemello, G.; Motta, A.; Sglavo, V.M. Nano-Hydroxyapatite Derived from Biogenic and Bioinspired Calcium Carbonates: Synthesis and in Vitro Bioactivity. *Nanomaterials* **2021**, *11*, 264. [CrossRef] [PubMed]
75. Akobundu, U.U.; Ifijen, I.H.; Duru, P.; Igboanugo, J.C.; Ekanem, I.; Fagbolade, M.; Ajayi, A.S.; George, M.; Atoe, B.; Matthews, J.T. Exploring the Role of Strontium-Based Nanoparticles in Modulating Bone Regeneration and Antimicrobial Resistance: A Public Health Perspective. *RSC Adv.* **2025**, *15*, 10902–10957. [CrossRef] [PubMed]
76. Ngece, K.; Khwaza, V.; Paca, A.M.; Aderibigbe, B.A. The Antimicrobial Efficacy of Copper Complexes: A Review. *Antibiotics* **2025**, *14*, 516. [CrossRef]
77. Golovchak, R.; Mahlovanyi, B.; Shpotyuk, Y.; Kus-Liskiewicz, M.; Kozianska, J.; Zadrag-Tecza, R.; Zagula, G.; Trzyna-Sowa, M.; Kovalskiy, A.; Gala-Bladzinska, A.; et al. Copper Strontium Phosphate Glasses with High Antimicrobial Efficacy. *Sci. Rep.* **2025**, *15*, 4677. [CrossRef]
78. Safarova, Y.; Nessipbekova, A.; Syzdykova, A.; Olzhayev, F.; Umbayev, B.; Kassenova, A.; Fadeeva, I.V.; Askarova, S.; Rau, J.V. Strontium- and Copper-Doped Ceramic Granules in Bone Regeneration-Associated Cellular Processes. *J. Funct. Biomater.* **2024**, *15*, 352.

79. Wan, B.; Wang, R.; Sun, Y.; Cao, J.; Wang, H.; Guo, J.; Chen, D. Building Osteogenic Microenvironments with Strontium-Substituted Calcium Phosphate Ceramics. *Front. Bioeng. Biotechnol.* **2020**, *8*, 591467. [CrossRef]
80. Alashi, S.; Alkhouri, I.; Alghoraibi, I.; Kochaji, N.; Houri, A.; Karkoutly, M. Evaluating Various Properties of Nanohydroxyapatite Synthesized from Eggshells and Dual-Doped with Si^{4+} and Zn^{2+}: An in Vitro Study. *Heliyon* **2024**, *10*, e35907. [CrossRef]
81. Li, J.; Zhang, T.; Liao, Z.; Wei, Y.; Hang, R.; Huang, D. Engineered Functional Doped Hydroxyapatite Coating on Titanium Implants for Osseointegration. *J. Mater. Res. Technol.* **2023**, *27*, 122–152. [CrossRef]